Bubble Dynamics on Structured Surface in Microchannel

by
Siyu Chen

Submitted to the Department of Mechanical Engineering in

Partial Fulfillment of the Requirements for the

Degree of Master of Science in Mechanical Engineering

at the

Massachusetts Institute of Technology

June 2013

Signature of Author: _____
Department of Mechanical Engineering
May 10, 2013

Certified by: _____
Evelyn N. Wang
Associate Professor of Mechanical Engineering
Thesis Supervisor

Accepted by: _____
David E. Hardt
Chairman, Department Committee on Graduate Theses

Bubble Dynamics on Structured Surface in Microchannel

By
Siyu Chen

Submitted to the Department of Mechanical Engineering on May 10, 2013,
in Partial Fulfillment of the Requirements for the
Degree of Master of Science in Mechanical Engineering

Abstract

Surface enhancement is a potential way to improve the performance of flow boiling in microchannels, which is considered to be one of the most promising cooling methods to solve thermal management challenges faced by future semiconductor products. Considerable research has been done on examining the functions of engineered surfaces. However, the mechanism of how these surfaces improve the flow boiling performance is still unclear.

In this thesis, bubble dynamics on micropillar array surfaces were studied. A surface energy based model is presented to predict the bubble morphology on pillar array surfaces. The results showed that bubbles tend to stay on top surfaces of pillars at solid fractions greater than 0.162, keeping liquid films underneath the bubbles. On the other hand, on surfaces at solid fraction less than 0.162, bubbles tend to propagate within the pillar unit cells.

A flow loop with good degassing and a fluid temperature control system was designed and built for various flow boiling experiments. Five different types of silicon micropillar array surfaces were fabricated. Moreover a setup for observing bubble dynamics in microchannels under flow boiling conditions was developed. Experiments were performed to investigate the bubble dynamics on silicon micropillar array surfaces. Bubble departure modes were observed. The bubble departure size of direct departing mode was found to be independent with flow rate while departure size of sliding mode decreased with increasing of the flow rate. Three potential methods to create single nucleation sites for improved studies of bubble dynamics were also presented in this thesis.

An experimental setup to investigate behavior of a single bubbles created by air injection on micropillar array was presented. Single 10-30 μm injection holes were fabricated on micropillar array surfaces by laser cutter. The experimental results show that structured surfaces have higher bubble departure sizes than that for a plain surface. The surfaces with solid fractions greater than 0.162 had larger departure sizes than that of surfaces with solid fractions smaller than 0.162 at mass flow rates above 250 kg/m^2s while departure sizes of the higher solid fraction surfaces become smaller than that of lower solid fraction surfaces when flow rates decreased below 200 kg/m^2s. The similarity between the departure sizes obtained by air injection experiments and flow boiling experiments suggest that air injection experiments

could provide useful information on understanding the vapor bubble departure behavior on micropillar array surfaces. Silicon micropillar array surfaces may have larger bubble departure sizes than plain surfaces, however, the surfaces with solid fractions greater than 0.162 are suggested for boiling due the a large amount of liquid thin films may create for higher heat transfer rates.

Thesis Supervisor: Evelyn N. Wang
Title: Associate Professor, Mechanical Engineering

Table of Contents

List of Figures

List of Tables

Chapter 1

Introduction

1.1 Motivation

Thermal management has become one of the critical limitations for the development of semiconductor products. For example, the high-concentration photovoltaic (HCPV) solar cells were developed in order to enhance the optoelectronic transition efficiency and reduce the cost of solar cell systems at the same time. However, the HCPV cells also generate significant amounts of heat during the solar energy to electrical energy conversion. So far, the highest conversion efficiency of HCPV solar cells is around 42%, which are developed by Boeing Spectrolab [1]. This means, about 60% concentrated solar radiation is converted into the form of heat. Under a typical concentration of 1500 suns, the generated heat flux can reach as high as 120 W/cm^2. If this heat cannot be dissipated effectively, the cell temperature will dynamically increase, which will lower the energy-conversion efficiency [2-3] and may even cause burn out of the device.

Computer integrated circuit (IC) technologies are also facing such thermal management challenges. According to a review article by Pop, the power densities of commercialized computer chips already reach 100 W/cm^2 [4] and predicted by Krishnan *et al.*, the power density of semiconductor-microarchitecture can reach as high as 1000 W/cm^2 in the near future [5]. Under such extreme heat dissipation conditions, traditional air-cooling methods or single phase liquid cooling method can no longer sufficiently cool the devices. Therefore, developing a more efficient cooling method is very important to meet the thermal management requirements for future semiconductor-devices.

1.2 Backgrounds

Flow boiling in microchannels is one of the most promising cooling methods for cooling the high energy-density devices such as solar cells and computer chips. The advantage of this cooling method is utilizing the high surface area to volume ratio of microchannel and high latent heat capacity of working fluid to achieve higher heat removal from devices. It is also able

to provide uniform cooling across the devices due to the steady temperature during the boiling process.

However, the actual performance of flow boiling in microchannel cooling is limited by the critical heat flux (CHF), which indicates the maximum heat that a device can dissipate through this cooling method. Heat generation beyond the CHF will cause rapid increase of device temperature and may even cause device burn out. Therefore, it is very important to obtain a complete CHF data set and fully understand the CHF mechanism before applying flow boiling in practical applications.

Many research studies have been conducted to investigate CHF data for various micrchannels in various flow conditions. Mukherjee *et al.* developed a pumpless loop system to cool the hot devices with FC-72 [6]. The loop system consists of two parallel vertical tubes and relied on the fluid density difference between those two tubes to drive the fluid motion. The heated copper surfaces with micro-fin enhancement were integrated into one tube with dimensions of 21.3 x 21.3 cm^2. The height of the microchannel varied from 0.13 mm to 12.32 mm. The CHF values reported ranged from 25.5 W/cm^2 to 62 W/cm^2. Their experimental results showed that the smaller microchannels have higher CHF value and it can be further enhanced by micro-fin structures compared to a plain surface.

Qu *et al.* fabricated 21 parallel rectangle microchannel arrays on a 4.48 cm X 1.0 cm oxygen-free copper block [7]. Each microchannel had a width of 215 μm and a height of 821 μm. The deionized water was driven by a gear pump through the microchannel heat sink at various mass flow rates from 86 to 368 kg/m^2s. The CHF data were measured at two difference water inlet temperature conditions: 30 °C and 60 °C. The reported effective CHF data ranges from 107.64 to 216.76 W/cm^2 and as expected, the CHF increased with increasing flow rate. They also observed the strong vapor backflow when heat flux approaches CHF and they claimed that this is caused by the amplification of the parallel channel instability near the CHF condition. They believed that vapor backflow was the main reason why they did not see much change in CHF for different water inlet temperature because the backward vapor flow led to the loss of subcooling.

Wojtn *et al.* attempted to establish a more complete CHF data set for the saturated flow boiling of R-134 and R-245fa in single microchannels with inner diameters of 0.5 mm and 0.8 mm [8]. They have developed a flow boiling loop, which was able to control the flow rate, refrigerant saturation temperature, heated length and liquid subcooling. A series of experiments were performed at different flow conditions that can be controlled by the loop. The reported CHF data for R-134a ranged from 12 W/cm^2 to 60 W/cm^2 and the CHF data for R-245fa was from 175 W/cm^2 to 450 W/cm^2. They found that the CHF was influenced by flow mass velocity, heated length, microchannel dimension and fluid property. However, no obvious influence of subcooling was found.

A great number of research studies have focused on CHF of flow boiling in microchannels where numerous CHF data were reported for various working fluids and flow conditions. However, the acquired CHF data are still not close enough to heat dissipation requirement for the future high power density devices, which is 1000 W/cm^2. Therefore, many efforts examined factors that caused CHF and investigated methods to improve the CHF. One of the common conclusions is that flow instability plays an important role on CHF of flow boiling in microchannel.

Bergles *et al.* reviewed existing CHF experiements for flow boiling in microchannel and summarized two major flow instabilities that affect CHF [9]. One of the instabilities is upstream compressible volume. As proposed in the paper of Boure *et al.* [10], when there is a compressible volume upstream of the heated section, significant pressure drop oscillations will occur, which may lead to CHF. The other type of instability is excursive instabilities Kuo *et al.* further extended these types of instabilities by adding two models: rapid bubble expansion and CHF instability [11]. This phenomenon is much more common in microchannels because the nucleated vapor bubbles experienced much faster growth rates under extremely high heat fluxes in such small confined spaces. The growth rate could be fast enough to suppress the upstream flow and cause large pressure drop oscillations. Under such conditions, certain heated area could experience a shortage of liquid supply and cause significant increase of device temperature, which would lead to CHF.

Past research has proposed methods to suppress these instabilities by increasing the upstream pressure. The most common method to achieve this is adding inlet restriction. Kandlikar *et al.* experimentally studied the pressure drop elements (inlet restriction) on the flow instability of flow boiling in microchannel [12]. Six parallel microchannels with rectangular cross section were machined on a copper block. Each microchannel has a hydraulic diameter of 333 μm and a length of 63.5 mm. Two different inlet restrictions with the 51% and 4% area of the cross-sectional area were added at the inlet of each microchannel. They investigated the videos and pressure drop oscillation data recorded during the flow boiling experiment and compared the results to their previous work, they found that 51% inlet restriction partially stabilized the flow but could not completely eliminate flow reversal. In the case of 4% inlet restriction, flow instability was completely eliminated, but at the same time, a significantly larger pressure drop was required to drive the flow in the microchannel.

Kosar *et al.* fabricated five parallel microchannels on the silicon wafer by photolithography and deep reactive ion-etching (DRIE) [13]. The dimensions of the microchannels are 200 μm in width and 264 μm in depth. 20 μm wide inlet restrictors with various lengths were incorporated at the inlet of each microchannel. They experimentally studied how inlet restrictors affected the flow boiling performance of water. Their results agreed with previous results that inlet restrictors could eliminate the vapor backwards flow and stabilize the boiling flow. They also successfully correlated the onset of unstable boiling (OUB) heat flux q''_{oub} and the pressure drop multiplier M, which is defined in Eq. 1.1. They found that OUB heat flux increased with increasing M, which indicated that with more flow restrictions at the inlet of microchannels, better boiling performance can be achieved.

$$M = \frac{\Delta P_{microchannel+}\Delta P_{orifice}}{\Delta P_{microchannel}} \tag{1.1}$$

Park *et al.* further studied the effects of inlet restrictors on CHF of flow boiling for three refrigerants: R134a, R236fa and R245fa [14]. Two microchannel heat sinks consisting each of 20 parallel rectangular microchannels were tested: one had microchannels with 467 μm width and 405 μm depth, the other had microchannels with 199 μm width and 765 μm depth. 300 μm

circular orifices were used for 467 μm wide microchannels and a rectangular slit with 200 μm in height was used for 199 μm wide microchannel to stabilized boiling flow. They measured the boiling curve and CHF data at various flow rates. Their results indicated that orifices were able to initiate boiling in microchannel at lower heat flux due to the high pressure drop they create and CHF values were improved at high flow rate. However, little improvement was observed in lower flow rate. No explanation was provided for this phenomenon, the little improvement on CHF may be caused by the less pressure drop the orifices create at low flow rates.

Many studies have shown that inlet restrictors can stabilize boiling flows and improve flow boiling performance. However, it may consume additional power to maintain same mass flow rate through restrictors compare to that without restrictors. Implementing inlet restrictors may work for applications where power consumption is not the limitation to achieve better performance. However, it can possibly become an issue when considering the applications in aerospace, where power is not sufficient; or applications such as cooling of solar cells, where tradeoff between how much more power it gains from better cooling system and how much power is put in to run the cooling system is a major concern.

Surface modifications promise heat dissipation performance by mitigating flow instabilities. Kandlikar reviewed existing models on nucleation criteria of the cavity size and put forward a statement that with suitable design of cavity size, the wall superheat that initiates the nucleation can be reduced, which leads to a lower vapor pressure inside the bubble [15]. Thus, the quick bubble expansion can be suppressed and the flow instability can be eliminated.

Kuo *et al.*'s experimental results well-supported Kandlikar's model incorporating the role of nucleation sites on flow boiling [16]. They used devices with five parallel, 10 mm long, 200 μm wide and 253 μm deep microchannels, which were fabricated on silicon by photolithography followed by reactive ion etching (RIE) and deep reactive ion etching (DRIE). Two different types of reentrant cavities were added to the side walls of each microchannel, as shown in Figure 1-1. One had a 7.5 μm mouth and 25 μm inside diameter reentrant body. Reentrant bodies were separated from each other. The other type of cavities has same dimension but with the interconnected reentrant bodies. They also had the plain wall for

comparison. The flow boiling experiments were running at different flow rates from 86-520 kg/m^2s. Their results well-indicated that good cavities were able to reduced onset nucleation boiling (ONB) wall temperature as well as ONB heat flux. They also measured the local wall temperature for the post onset flow oscillation (OFO) boiling. Their results showed that the devices with cavities had longer stable boiling region in terms of heat flux, which means flow instability were suppressed. Because of the extended stable boiling region, the CHF therefore was increased about 15-33%. The maximum CHF value that obtained in their work was about $200W/cm^2$ at a flow rate of 520 kg/m^2s.

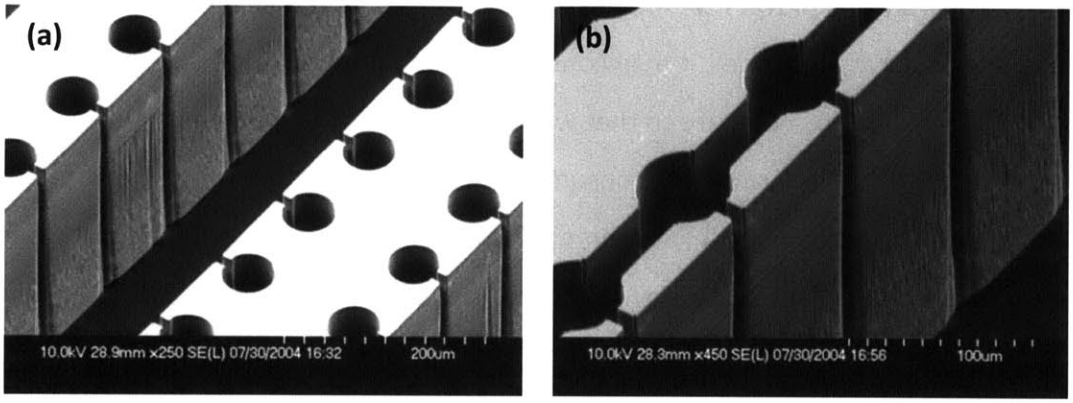

Figure 1-1 SEM images of microchannels with cavities. A. Kosar, C. Kuo and Y. Peles, *Suppression of Boiling Flow Oscillations in Parallel Microchannels by Inlet Restrictors*, Journal of Heat Transfer, 2006. (a) Nonconnected reentrant cavity microchannel (b) Interconnected reentrant cavity microchannel.

Li *et al.* studied flow boiling performance in nanowire-coated microchannels [17]. In their work, *in situ* silicon nanowires incorporated inside the 20 mm long, 250 μm wide and 200 μm deep microchannel arrays. Boiling curves, local wall temperature and pressure drops through microchannels were measured at various flow rates from 119 to 571 kg/m^2s. Heat transfer coefficients were also calculated based on the measurement data. It was found that nanowire-coated microchannels successfully reduced the ONB wall temperature and delayed the OFO. Significantly smaller fluctuations of pressure drop and wall temperatures were observed for silicon nanowire enhanced surface compared to plain surface. Improvement of Heat transfer coefficient was also observed. The improvement was attributed to the structures

of nanowires, which provided sufficient nucleation sites to lower the wall superheat of boiling and suppressed the flow instability.

While designing nucleation sites are important for the initial stage for bubble formation, it is also very important to investigate the bubble growth and departure behavior after bubble nucleation. If the nucleated bubbles are not being removed efficiently, the bubbles still could grow and block the channel, which eventually leads to the upstream compressible volume instabilities. Numerous studies have investigated bubble dynamics during flow boiling in microchannels. Lee *et al.*, explored the bubble dynamics in both single and two parallel trapezoid microchannels [18-19]. Each microchannel had a hydraulic diameter of 41.3 μm and a length of 28 mm. They measured the sizes of signal bubble and bubble slug during their growing process and found a linear dependence of bubble size on time for the single bubble and an exponential dependence on time for the bubble slug. The higher growth rate of slugs could be explained by thin film evaporation, which was the dominating heat transfer mechanism during slug evolution. They also observed some unusual bubble grow processes, which could not be explained by existing theories. In their papers, the bubble departure sizes were measured as well. Their results showed that the departure size was governed by the surface tension and drag of bulk flow. It was also found that the traditional frequency and departure diameter relationship was not applicable in their microchannel studies.

Kuo *et al*, however, concluded that the products of frequency and departure diameter might still be constant for microchannels. They studied the bubble dynamics of flow boiling in five parallel microchannels with interconnected reentrant cavities on side walls (similar cavities were shown in Figure 1-1b) [20]. They measured the bubble departure diameters and corresponding departure frequencies and found that the products of frequency and departure diameter kept constant, which was similar to the macroscale. The difference was that the value of these products in microchannel was an order of magnitude smaller.

Although considerable research has focused on bubble dynamics of flow boiling in microchannels, common conclusions have not been reached yet. On the other hand, few research studies have focus on the bubble dynamics on structured surfaces and the actual

mechanism of bubble growth and departure is still unclear. Therefore, it is necessary to conduct research on bubble dynamics on structure surface under flow boiling conditions, to explore how the bubble grow and departure on the structured surface and understand how structured surface improve the flow boiling performance.

1.3 Objective and Outline

The objective of this thesis is to study the bubble dynamics on structured surfaces, to investigate the role of structures in bubble growth and departure behaviors and to understand how structures affect flow boiling performance in microchannels. The outline of this thesis is shown below:

In Chapter 1, the motivation for studying flow boiling in microchannel and bubble dynamics on well-defined-structured surfaces is presented. A brief literature review was done to show the state of the art for flow boiling in microchannel.

In Chapter 2, a model based on surface energy analysis was developed to predict the bubble morphology for pillar array surfaces with different surface geometries.

In Chapter 3, the design and implementation of the experimental flow boiling loop was presented.

In Chapter 4, the flow boiling experiments to explore the bubble dynamics on micropillar array silicon surfaces were conducted. A test setup to observe bubble dynamics in microchannels in a side view was demonstrated in this chapter.

In Chapter 5, the departure behaviors of single bubble created by air injection from backside of micropillar array silicon surface were studied. Experiments of observing the bubble departure process in a side view was presented.

In Chapter 6, the conclusions of this thesis and the potential future works were presented.

Chapter 2

Bubble Morphology on Structured Surface

When the channel size is reduced to the microscale, the surface tension plays a very important role on the bubble dynamics. It affects the bubble nucleation, growth and departure process. Surface tension also affects the bubble morphology on surfaces, which is usually shown as changing of the contact angles. When structured surfaces are introduced, the bubble morphology becomes much more complicated. It is critical to understand the bubble morphology on different structures because it indicates how bubble interact with surfaces, which could influence the overall surface tension on the bubble, the heat transfer area and even the heat transfer mechanism. As a result, it affects the bubble departure and flow boiling performance. Therefore, as the first step, the bubble morphology is studied.

We used micropillar array surfaces for our studies for the following reasons: First, the micropillar array surfaces are well controlled that surface properties such as roughness and solid fraction can be obtained from the pillar diameter, height and spacing, which facilitates modeling efforts to provide insights into how different surface properties affect bubble dynamics in microchannels. Second, the standard procedures have been established for fabricating micropillar arrays on silicon material by photolithography and deep reactive ion etching (DRIE). This makes it easy to interface with the potential applications such as computer chips, which are usually made from silicon. The details of the micropillar arrays on silicon substrate will be discussed in section 4.1.

2.1 Modeling

Firstly, the case that the bubble nucleates at the bottom of the pillar is studied. The bubble is simplified as a thin layer of vapor bubble that fills the bottom of a unit form by four pillars. The schematic drawing for this case is shown in Figure 2-1

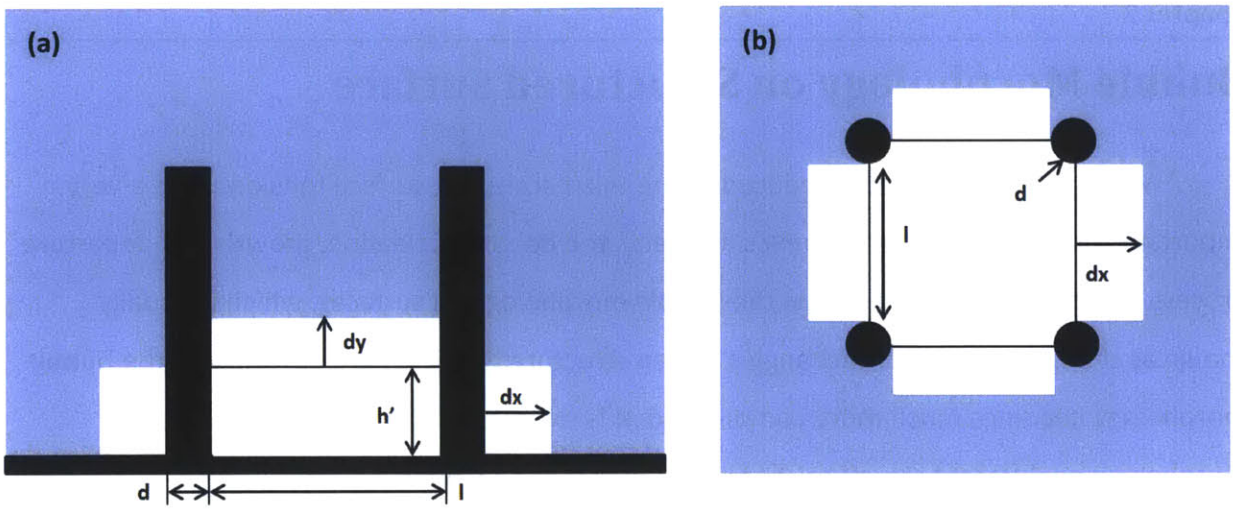

Figure 2-1 Schematic showing (a) Cross section view of bubble nucleation at bottom of the pillars with an initial height of h' (b) Top view of the bubble nucleation at bottom of the pillars within a unit cell formed by four pillars; where d is the diameter of pillar and l is the edge to edge pillar spacing.

Assume that the height of the original bubble in the unit cell is h'. Two potential growth directions can be seen in the figure: one is growing dy upwards and the other is growing dx laterally to fill the adjacent units. The surface energy change due to the bubble growing laterally in a length of dx can be calculated by the following equation:

$$\Delta E_x = 4\gamma_{SV} l dx + 4\gamma_{LV}(2h' + l)dx - 4\gamma_{SL} l dx \,. \qquad \text{(Eqn 2.1)}$$

The surface energy change due to the bubble growing upwards in a length of dy is:

$$\Delta E_y = \gamma_{SV}\pi d dy + \gamma_{LV} 4l dy - \gamma_{SL}\pi d dy \,; \qquad \text{(Eqn 2.2)}$$

where γ_{SV}, γ_{LV} and γ_{SL} are the surface energies of solid-vapor, liquid-vapor and solid-liquid interfaces. l is the spacing length between two pillar as shown in Figure 2-1. d is the diameter of each pillar and h' is the height of the original bubble in the unit cell before it begin to grow. The range of h' from 0 to the height of pillar, is represented by h.

By comparing the energy changes in x and y direction, the preferable growth direction can be determined since the bubble always grows in the direction that has the

lower energy state. For easy comparison, a dimensionless energy term is defined as shown in Eq. 2.3:

$$\Delta E_i^* = \frac{\Delta \mathrm{E}_y}{\Delta \mathrm{E}_x} = \frac{\gamma_{SV}\pi d + \gamma_{LV} 4l - \gamma_{SL}\pi d}{4\gamma_{SV} l + 4\gamma_{LV}(2h' + l) - 4\gamma_{SL} l} \cdot \frac{dy}{dx} \ . \qquad (Eqn\ 2.3)$$

By applying the constant growth volume constraint, the relationship between *dy* and *dx* can be obtained, as shown in Eq. 2.4:

$$\left[(l+d)^2 - \frac{\pi}{4} d^2\right] dy = 4h' l dx \ . \qquad (Eqn\ 2.4)$$

Substituting the Eq.2.4 into the Eq.2.3 and rearranging the equation, the $\Delta \mathrm{E}_i{}^*$ can be expressed by the Eq. 2.5:

$$\Delta E_i^* = \frac{\pi d \frac{\gamma_{SV} - \gamma_{SL}}{\gamma_{LV}} + 4l}{l \frac{\gamma_{SV} - \gamma_{SL}}{\gamma_{LV}} + (2h' + l)} \cdot \frac{h' l}{\left[(l+d)^2 - \frac{\pi}{4} d^2\right]} \ . \qquad (Eqn\ 2.5)$$

Noticing that $(\gamma_{SV} - \gamma_{SL})/\ \gamma_{LV} = \cos\theta_Y$, where θ_Y is Young's contact angle, Eq. 2.5 can be further simplified, shown in Eq. 2.6:

$$\Delta E_i^* = \frac{\pi d \cos\theta_Y + 4l}{[l\cos\theta_Y + (2h' + l)]} \cdot \frac{h' l}{\left[(l+d)^2 - \frac{\pi}{4} d^2\right]} \ . \qquad (Eqn\ 2.6)$$

For a hydrophilic surface, such as the silicon surface with oxide layer, the Young's contact angle will be less than 90°. Thus a positive surface energy change will be obtained for a bubble growing in both x and y directions. Considering this fact, the criteria to determine which direction the nucleated bubble prefers to grow can be achieved: if $\Delta E_i^* > 1$, the bubble tends to grow horizontally; if $\Delta E_i^* < 1$, the bubble tends to grow vertically.

When the bubble just starts growing inside the unit, which corresponding to $h' \to 0$, the value of ΔE_i^* is infinitely small. This means the nucleated bubble will grow upwards to fill the unit at the early stage. The ΔE_i^* increases as the bubble grows inside a unit cell (h' increases). It reaches its maximum value when h' increases to h. Therefore, it is reasonable

to check the value of ΔE_i^* when $h' = h$ to determine whether the vapor bubble will propagate into the adjacent unit or keep growing upwards until it fills the whole unit. The ΔE_i^* at $h' = h$ for different micropillar array surfaces with various solid fraction and roughness are plotted in Figure 2-2. For the silicon pillar array surface, the roughness r and solid fraction φ are defined in terms of pillar diameter$d$, height h and spacing l, which are shown in Eq. 2.7 and Eq. 2.8:

$$\mathrm{r} = \frac{(l+d)^2 + \pi dh}{(l+d)^2} = 1 + \frac{\pi dh}{(l+d)^2} \qquad (Eqn\ 2.7)$$

$$\varphi = \frac{\frac{\pi}{4} d^2}{(l+d)^2}. \qquad (Eqn\ 2.8)$$

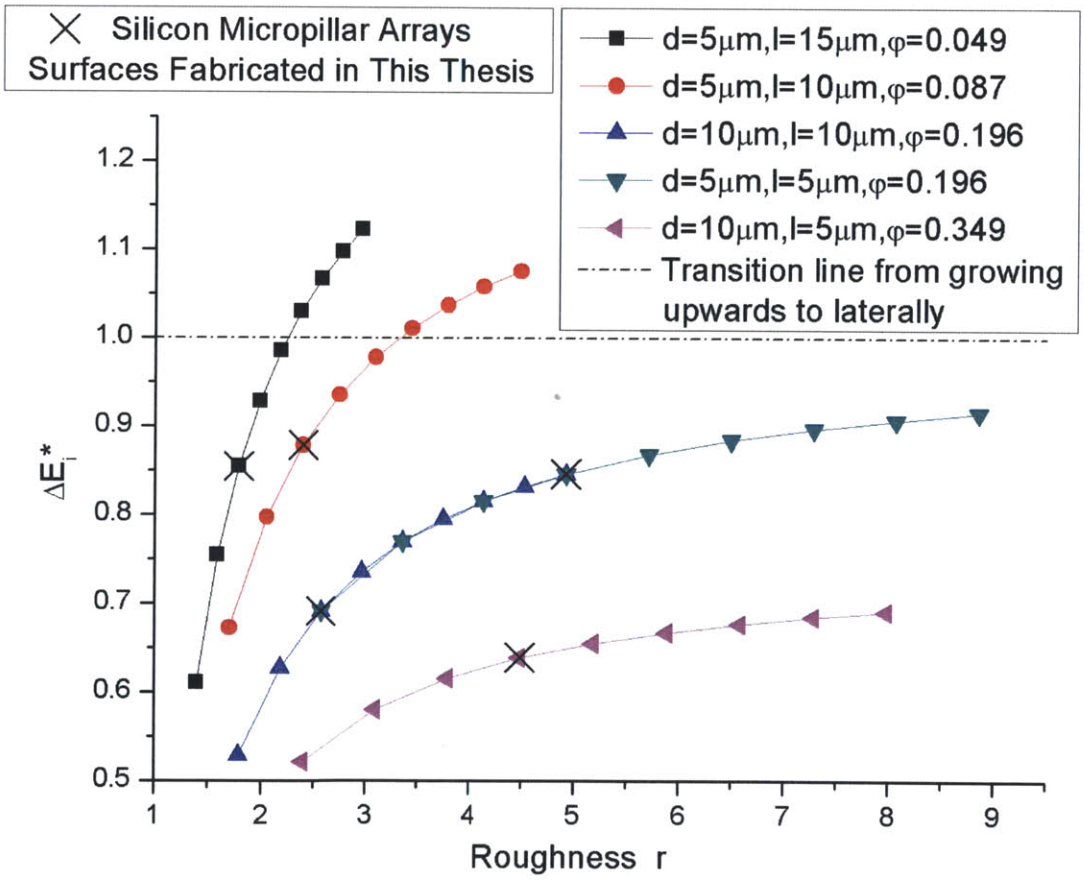

Figure 2-2: The values of ΔE_i^* at $h' = h$ for silicon pillar array surface with various solid fraction and roughness. Higher solid fraction surfaces have lower ΔE_i^* values and higher roughness surfaces have higher ΔE_i^* values

From Figure 2-2, the characteristics of ΔE_i^* plots are determined by solid fraction and roughness. Higher roughness will lead to higher ΔE_i^*. On the other hand, a higher solid fraction will suppress this increase, which means the surface with high solid fraction can suppress the bubble propagating inside the micropillars. For surface that has a ΔE_i^* value higher than 1, the bubble will start to grow laterally before it fills the whole unit. To determine how many units the bubble will fill before it reaches the top of pillars, the Eq. 2.6 is extended into a much more general form, as shown in Eq. 2.9:

$$\Delta E_n^* = P_n \Delta E_i^* ; \qquad (Eqn\ 2.9)$$

where the geometry factors P_n is related to the number of units that have been filled by vapor, whose value is listed in Table 2.1. ΔE_n^* compares the energy change for a bubble to grow upwards and the energy change for a bubble to grow laterally when it fills n pillar units. The smallest n that has $\Delta E_n^* < 1$ is the number of units that bubble will fill before it grows into the same height as the pillars.

Table 2.1 Geometry Factors P_n

No. of units	1	2	3	4	5	6
P_n	1	3/4	2/3	1/2	1/2	5/12

Next, the case that the water vapor fills the several units is considered. The purpose is to determine whether the water vapor prefers to grow upwards from the pillars or propagate laterally inside the pillars. The single unit is first considered here and then will be extended to a more general form. Figure 2-4 shows the schematic for this case. Following the similar energy analysis, the comparison between the energy change for a vapor bubble growing inside and outside the pillars is conducted.

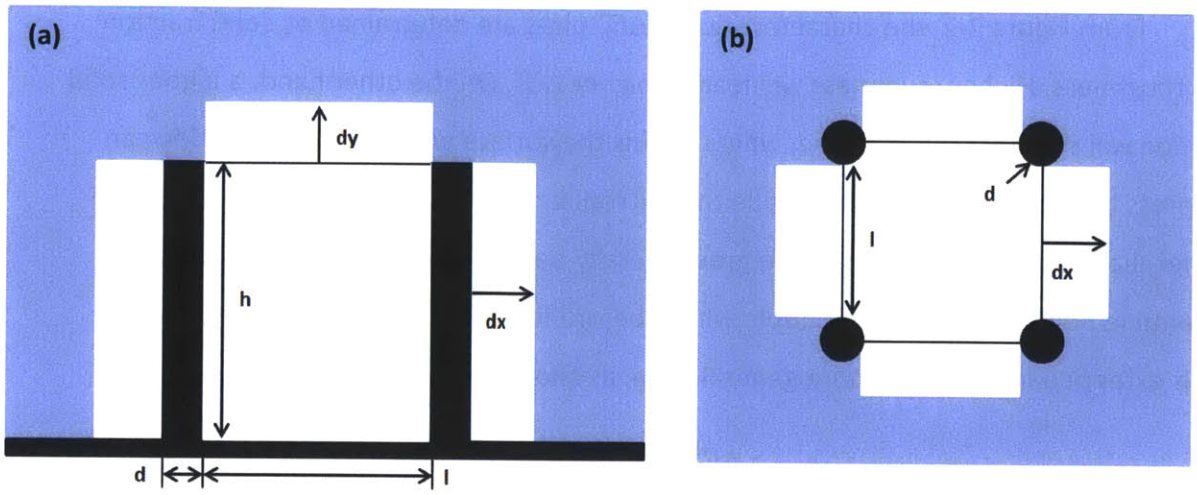

Figure 2-3 Schematic showing (a) Cross section view of bubble potential growing direction after filling the unit cell (b) Top view of bubble potential growing direction after filling the unit cell; where d is the diameter of pillar and l is the edge to edge pillar spacing.

The energy change for a bubble growing inside the pillars in a distance of dx can be calculated by Eq. 2.10. And the energy change for bubble growing in a distance of dy can be calculated by Eq. 2.11:

$$\Delta E_{inside} = \gamma_{SV} l dx + \gamma_{LV}(2h + l)dx - \gamma_{SL} l dx \qquad \text{(Eqn 2.10)}$$

$$\Delta E_{outside} = \gamma_{LV}(\pi d + 4l)dy. \qquad \text{(Eqn 2.11)}$$

We define a new dimensionless energy term by dividing $\Delta E_{outside}$ by ΔE_{inside} to determine the preferable growth direction. Young's equation and constant volume constraint are applied to simplify the equation and a final expression for this new dimensionless term is shown in Eq. 2.12:

$$\Delta E_p^* = \frac{\pi d + 4l}{[l\cos\theta_Y + (2h + l)]} \cdot \frac{hl}{\left[(l + d)^2 - \frac{\pi}{4}d^2\right]}. \qquad (Eqn\ 2.12)$$

If $\Delta E_p^* > 1$, the bubble tends to grow inside the pillars; if $\Delta E_1^* < 1$, the bubble tends to grow upwards. The ΔE_p^* for surfaces with various roughness and solid fraction are plotted in Figure 2-4. Similar to the ΔE_1^*, the ΔE_p^* increases with increasing roughness and a

higher solid fraction can suppress this increasing trend, which indicates bubble prefers to grow upwards from the micropillars with a high solid fraction and low roughness. Surfaces with different pillar diameters and spacing but same solid fraction also follow the same trend for the ΔE_p^* value.

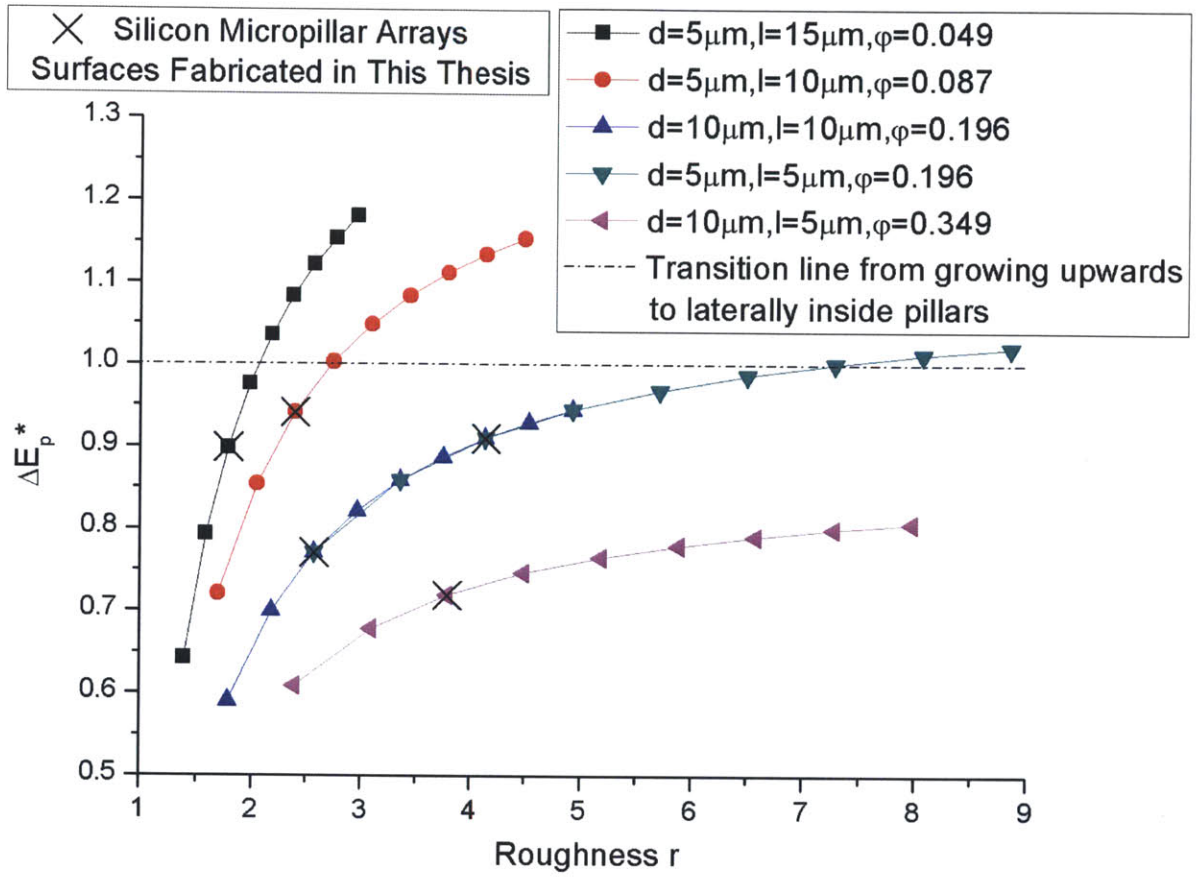

Figure 2-4: The values of ΔE_p^* for silicon pillars with various solid fraction and roughness. Higher solid fraction surfaces have lower ΔE_p^* values and higher roughness surfaces have higher ΔE_p^* values

In a third case, we considered the bubble filling one unit cell and growing upwards from micropillars. It is reasonable to predict that the liquid-vapor interface will advance on top of pillar surface until it researches the corner, as shown in Figure 2-5. There are two potential ways for the bubble to grow further. One is that the liquid-vapor interface start to grow downwards and the other is the liquid-vapor interface is pinned at the corner. In order to determine which growth direction the bubble prefers, we also used similar energy

analysis. Assuming that the liquid-vapor interface grow down in a length of dy. The energy change due to this interface movement can be calculated by Eq. 2.13:

$$\Delta \mathrm{E}_y = (\gamma_{SV} - \gamma_{SL})\frac{\pi d}{2}dy - \gamma_{LV} l dy\,. \qquad (Eqn\ 2.13)$$

Dividing both sides by $\gamma_{LV}(l+d)dy$, a dimensionless term can be obtained and defined as ${\Delta E_y}^*$. Replacing d and l by the solid fraction, a final expression can be obtained, shown in Eq. 2.14:

$${\Delta E_y}^* = \frac{\Delta \mathrm{E}_y}{\gamma_{LV}(l+d)dy} = cos\theta_Y\sqrt{\pi\varphi} + 2\sqrt{\frac{\varphi}{\pi}} - 1. \qquad (Eqn\ 2.14)$$

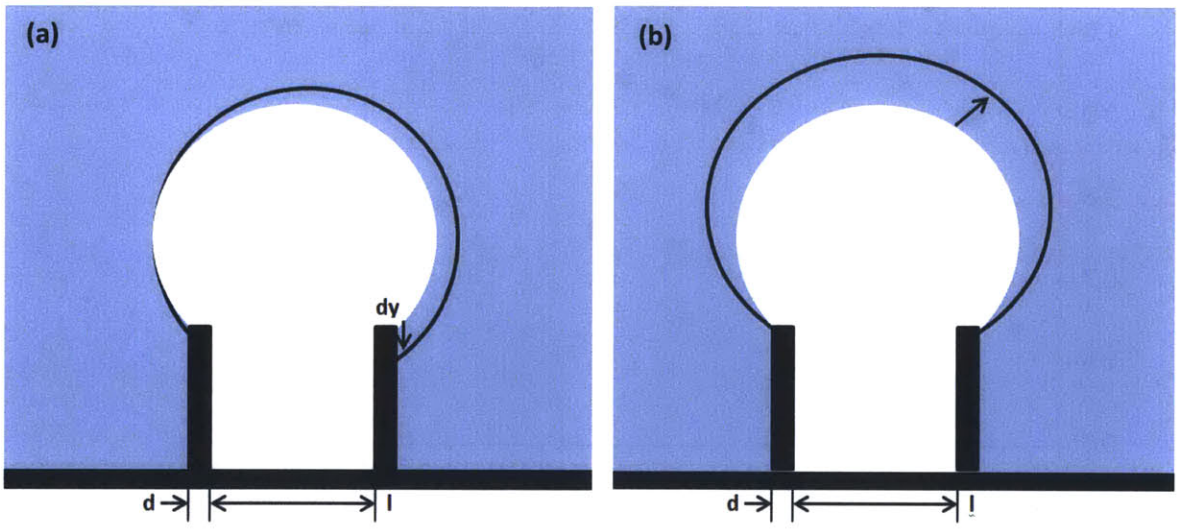

Figure 2-5 Schematic showing (a) bubble grows downwards after reaching the corner of the pillar (b) bubble grows with interface pinned at corner of the pillar; where d is the diameter of pillar and l is the edge to edge pillar spacing.

If ${\Delta E_y}^* < 0$, which means moving down the liquid-vapor interface, leading to a lower energy state, the vapor will soon cover the other side of the pillar and start to fill the next unit. A Wenzel bubble, which is defined as a bubble that fills the pillar unit cells, is much easier to form; If ${\Delta E_y}^* > 0$, the liquid-vapor interface will pin at the top corner until the interface reaches next pillar's top surface. In this case, a Cassie bubble, which is defined

as a bubble that stays on top of the pillars with a liquid layer underneath the bubble, is much easier to form. Therefore, a criterion to determine which type of bubble that is easier to form on the surface can be obtained. For the naturally oxidized silicon surface, the contact angle is approximately 40°, which results in a critical solid fraction of 0.162.

$$\varphi > \frac{1}{\pi cos^2\theta_Y + 4cos\theta_Y + \frac{4}{\pi}} \qquad \text{Cassie Bubble}$$

$$\varphi < \frac{1}{\pi cos^2\theta_Y + 4cos\theta_Y + \frac{4}{\pi}} \qquad \text{Wenzel Bubble}$$

In a fourth case, the bubble nucleate on top of the pillar is considered. The process is simplified as the bubble first nucleates on the top of one pillar and starts to grow until it reaches the nearby pillars. Here, homogeneous growth is considered and the bubble will first covers four pillar unit cells as shown in Figure 2-6. After this, bubble can keep growing above the pillars or start to grow down to fill the pillar unit cells. Similar energy analysis is done to determine which way is preferable for the bubble to grow.

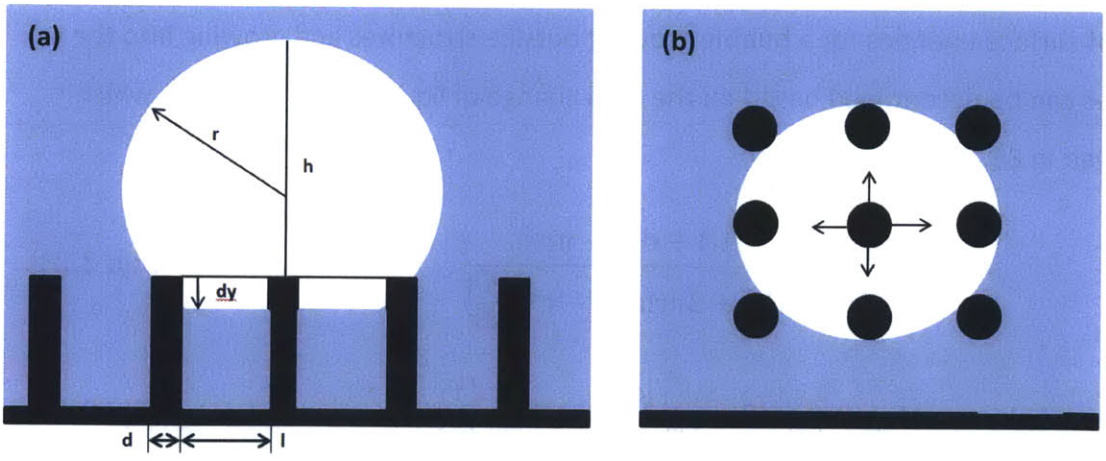

Figure 2-6 Schematic showing (a) cross section view of bubble nucleates on top of pillars (b) Top view of bubble nucleates on top of pillars and stay on four unit cells; where d is diameter of pillars, l is the pillar spacing, h is the height of the bubble and r is the radius of the bubble.

The energy changes for a bubble growing outside the structure with radius and growing downwards in a length of dy are compared. The relationship between bubble radius r and bubble height h is shown in Eq. 2.15; the volume and surface area of the bubble can be calculated as $V = \pi h^2(r - \frac{h}{3})$ and $S = 2\pi rh$. Base on this, simple relationships between change in volume and change in surface area due to the change in radius can be calculated, as shown in Eq. 2.16 and Eq. 2.17:

$$h = r + \sqrt{r^2 - p^2}, \qquad \frac{dh}{dr} = 1 + \frac{r}{\sqrt{r^2 - p^2}}, \qquad p = \frac{l + d}{2} \tag{Eqn 2.15}$$

$$\frac{dV}{dr} = \pi h^2 + 2\pi rh\frac{dh}{dr} - \pi h^2\frac{dh}{dr} \tag{Eqn 2.16}$$

$$\frac{dS}{dr} = 2\pi h + 2\pi r\frac{dh}{dr}\ . \tag{Eqn 2.17}$$

Consider the bubble grows down into the pillar units. Assuming it grow down by a length of dy, then the change of volume equals to $dV = (4(l + d)^2 - \pi d^2)dy$. This change of volume should equal to the volume change for a bubble growing outside the pillars in Eq. 2.16. Thus the relationship between dr and dy can be obtained as shown in Eq. 2.18. The change of surface energies for a bubble growing outside structures and growing into the structures can be determined based on the area change of liquid-vapor interface, which are showed in Eq. 2.19 and Eq. 2.20:

$$\frac{dr}{dy} = \frac{4(l + d)^2 - \pi d^2}{\pi h^2 + 2\pi rh\frac{dh}{dr} - \pi h^2\frac{dh}{dr}} \tag{Eqn 2.18}$$

$$\Delta E_u = \gamma_{LV} dS = \gamma_{LV}\left(2\pi h + 2\pi r\frac{dh}{dr}\right)dr \tag{Eqn 2.19}$$

$$\Delta E_d = (\gamma_{SV} - \gamma_{SL})4\pi d dy + \gamma_{LV} 8l dy\ . \tag{Eqn 2.20}$$

In this thesis, we defined a new dimensionless energy term ΔE_t^* to determine whether a bubble grows outside structures or inside structures by dividing ΔE_u by ΔE_d,

shown in Eq. 2.21. If $\Delta E_t^* > 1$, the bubble will grow into the structures; if $\Delta E_t^* < 1$, then the bubble will grow outside structures.

$$\Delta E_t^* = \frac{\Delta E_u}{\Delta E_d} = \frac{\gamma_{LV}\left(2\pi h + 2\pi r\frac{dh}{dr}\right)}{(\gamma_{SV}-\gamma_{SL})4\pi d dy + \gamma_{LV}8l}\frac{dr}{dy} = \frac{\left(\pi h + \pi r\frac{dh}{dr}\right)}{2\pi d cos\theta_Y + 4l}\frac{dr}{dy} \qquad (Eqn\ 2.21)$$

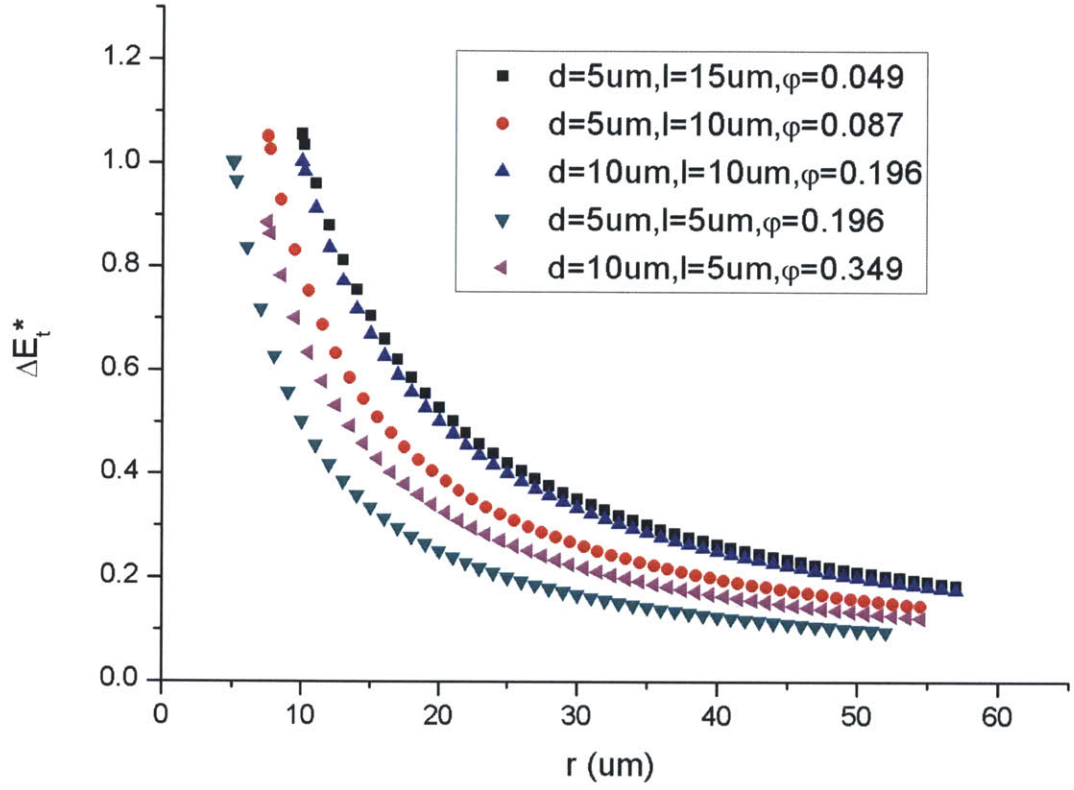

Figure 2-7 Values of ΔE_t^* for silicon pillar array surfaces with various solid fraction and roughness in terms of bubble radius.

Figure 2-7 shows the values ΔE_t^* for different pillar array surfaces. From the figure, the data points are all nearly lower than 1 except few points that have the values of radius very close to the spacing. These cases will not happen in practical scenarios because it requires the bubble to grow larger than the distance to reach the nearby pillars. Thus it can be concluded that a bubble that grows on top of the pillars will never grow down to fill the pillar units.

2.2 Chapter Summary

In this chapter, modeling work has been done to predict bubble morphology on micropillar array surface. By energy analysis, it is found that on high solid fraction surfaces, when a bubble nucleates at bottom of pillars, it tends to grow upwards to fill the pillar unit cell and starts to grow above the pillars; on the other hand, on low solid fraction surfaces, a bubble that nucleates at bottom of pillars will first propagate into several adjacent pillar unit cells before it start to grow above the pillars. It also has been found that the bubble will keep filling the pillar unit cells during its growth process on low solid fraction surface after it start growing above pillars, therefore a Wenzel bubble will form. On high solid fraction surfaces, the liquid-vapor interface will pin at top corner of the pillar and form a Cassie bubble. The critical solid fraction for silicon micropillar array surfaces to have a transition from Wenzel bubble preferable surface to Cassie bubble preferable surface has been found to be 0.162. The modeling work further showed that when a bubble nucleates on top of pillars, it will never grow down to fill the pillar unit cells.

Chapter 3

Flow Boiling Experimental Test Setup

To study the bubble dynamics in microchannel under flow boiling condition, a flow boiling loop is necessary to run various experiments. In this thesis, a flow loop was designed and built.

3.1 Flow loop

The schematic drawing of the built flow boiling loop is shown in Figure 3-1. As can be seen from the figure, the loop started with a peristaltic pump (L/S® Easy-Load® II pump head, Masterflex®), which provided constant flow rate ranges from 0.36 – 1000 mL/min. A flow meter (FLR1000 ST, Omega) was connected right after the peristaltic pump to measure the flow rate of the loop. After the flow meter was the pre-heater. The pre-heater was a coil made of copper tube and wrapped with high-temperature heat cable, where the water was preheated to a state close to saturated state. A thermocouple probe was added after the pre-heater to measure the water temperature after the pre-heater. A self-designed degassing tank was located after the pre-heater. The degassing tank was covered with several Kapton heaters controlled by an on/off controller. In the degassing tank, water was heated to a desired temperature and then pumped into the test fixture. More details on the degassing tank will be discussed in section 3.2. A high-temperature rope heater was wrapped on the copper tube between the degassing tank and the test fixture to prevent heat lost from natural convection. Different test fixtures for different experiments were placed after the rope heater wrapped tube and a differential pressure sensor was mounted on the fixture to measure pressure drop across the microchannel. Two thermocouple probes were added on the inlet and the outlet of the test fixture to measure the inlet and outlet flow temperatures. After the test fixture was a condenser. The condenser was a long copper tube with a fan placed on top of it. The fan provided constant air flow to cool the water inside the copper tube. After cooled by the condenser, the water was pumped back to the peristaltic pump and started a new cycle.

The voltage signals of the pressure sensors and the flow meter are acquired by an NI data acquisition (DAQ) board (USB 6211, NI) and then transfer to a LabView program, where the signals are converted into the actual pressure and flow rate measurements. The temperature signals from the thermocouple probes are collected by a digital thermocouple monitor (SR630, Stanford Research System) and then the collected temperature information is transferred to the Labview program through a GPIB cable. All the flow rate, pressure and temperature measurements were record by the Labview program every 1 second.

The test fixtures were placed on an inverted microscope (Eclipse Ti, Nikon), which was used to observe the bubble behaviors inside microchannel. The bubble dynamics was recorded by a high speed camera (Phantom v 7.1, Vision Research). The picture of complete flow boiling loop setup is shown in Figure 3-2.

To prevent contaminations, all components of the loop were cleaned by acetone, isopropyl alcohol (IPA) and DI water before they were assembled into the loop. The whole loop was also flushed by DI water before each experiment to ensure the clean experimental environment.

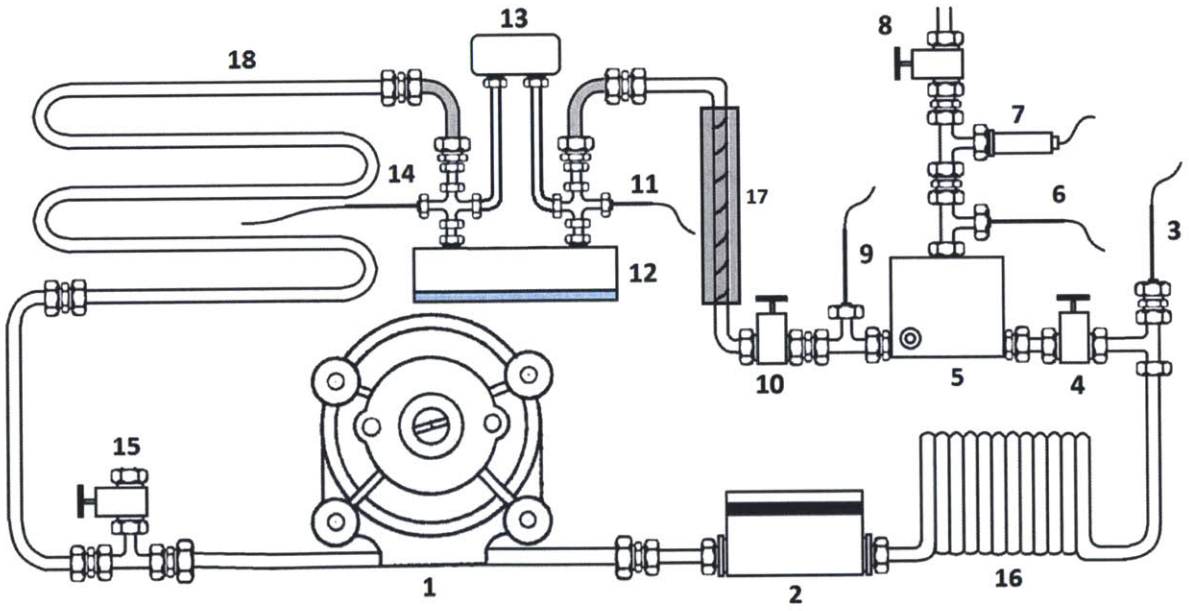

Figure 3-1 Schematic drawing of flow boiling loop. [1] Peristaltic pump [2] Flow meter [3, 6, 9, 11, 14] Thermal couple probes [4, 8, 10, 15] Vacuum valves [5] Degassing tank [7] Absolute

pressure sensor [12] Test fixture [13] Differential pressure sensor [16] Pre-heater [17] Post-heater [18] Condenser

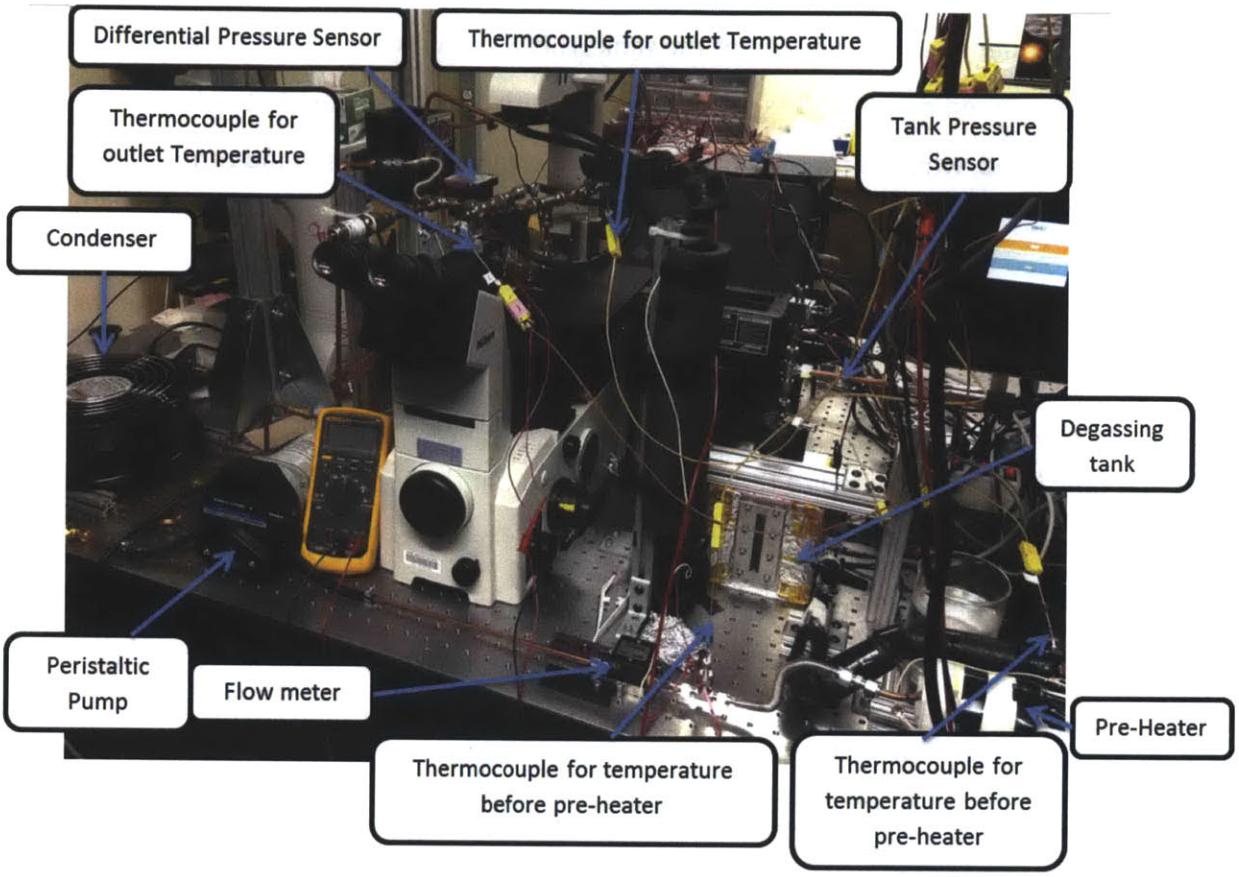

Figure 3-2 Flow boiling experimental setup

3.2 Degassing Tank and Degassing Procedure

Considerable amount of air may be either trapped inside the flow loop or dissolved in the deionized (DI) water, which will affect water nucleation and water vapor expansion inside microchannel. In order to capture the pure water vapor bubble dynamics, a degassing procedure is necessary before the experiment.

Water degassing can be achieved by the degassing tank. The design of the degassing tank is shown in Figure 3-3. The degassing tank is a cubic tank made of stainless steel. One port is located on top of the tank, which is designed for pressure sensor. This port also allows air or water vapor to vent and release the pressure inside. Inlet and outlet ports are located at two

sides of the tank. A narrow rectangular window is implemented on the front side of the tank, which is used for observing the water level inside. The observing window is covered by a polycarbonate sheet with O-ring sealing and was fixed on the tank by a stainless steel plate. A large window is opened at the bottom of the tank. This window is designed for cleaning purpose and is covered by a stainless steel mounting with O-ring sealing. At the backside of the tank, a port is added, where a thermocouple is inserted to measure the liquid temperature inside. The details about dimensions of the degassing tank can found in Appendix A.

The tank is covered by several Kapton heaters, which are able to heat the water inside. These Kapton heaters are connected to an On/Off controller (CN7800, Omega), which is connected to a power supply. The thermocouple probe that measures the water temperature inside the tank is also connected to the On/Off controller. If the temperature measurement from the thermocouple probe is greater than the desired temperature, the controller will shut the power of the Kapton heaters. Otherwise, the Kapton heaters will keep heating the tank. By this way, the degassing tank can heat the water to a desired temperature. The schematic drawing of degassing tank and heating control wiring diagram is shown in Figure 3-4.

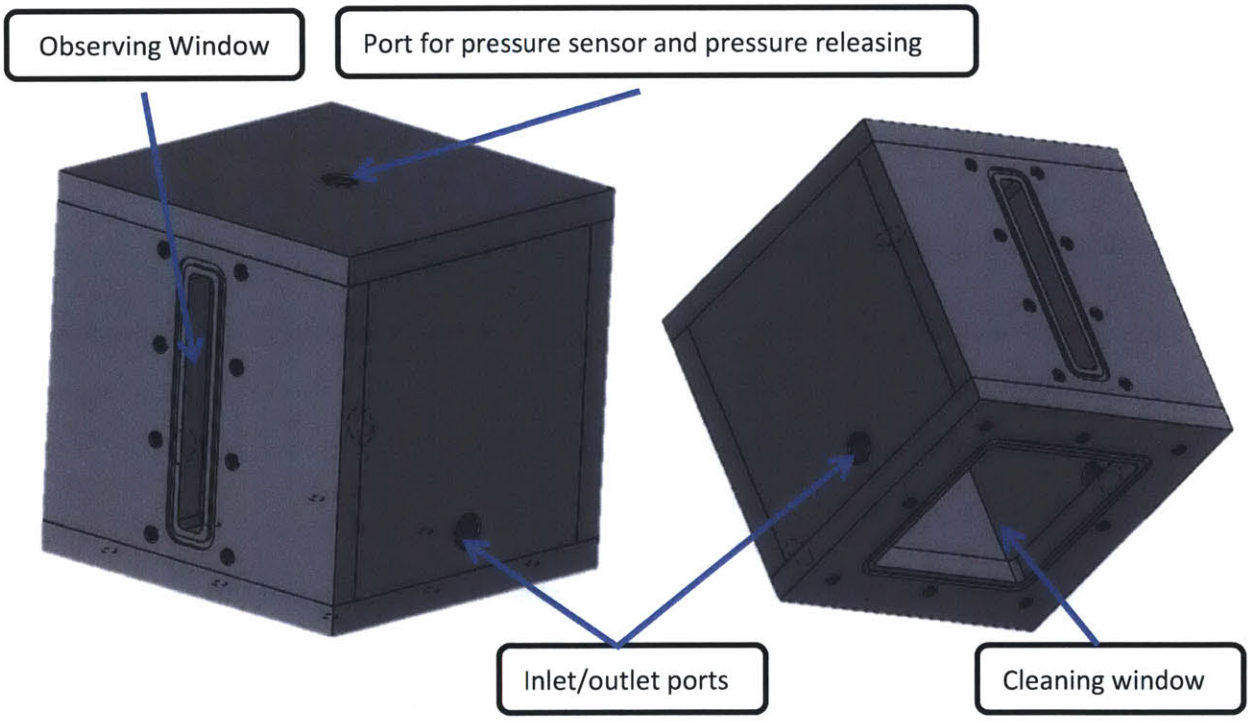

Figure 3-3: Design of the degassing tank.

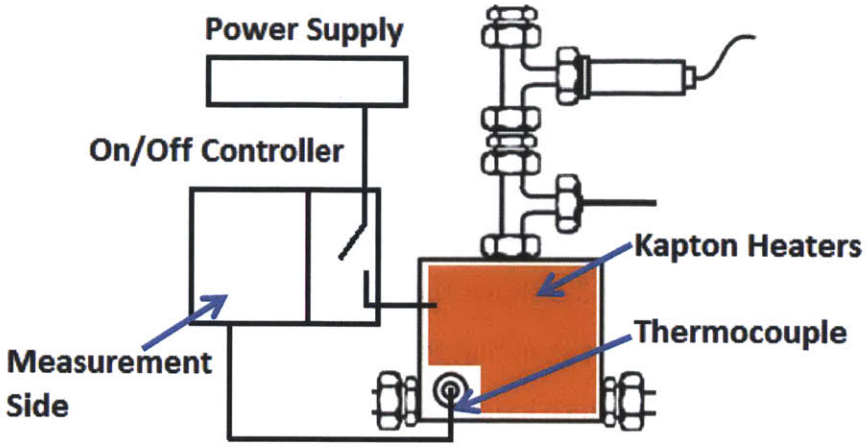

Figure 3-4 Heating control diagram of degassing tank

The following steps show the degassing procedure that was used in this thesis.

(1) Heat the water inside the tank to 105 °C with valves 4,8 and 10 closed (valves' location can be found in Figure 3-1).

(2) Open the valve 8 when pressure inside the tank increases to 140 kPa or stabilizes at more than 120 kPa.

(3) Close the valve 8 when the pressure inside the tank goes blow the 110 kPa and the Kapton heaters will start heating the water again.

(4) Repeat the step 2 and step 3 for 5 times.

By conducting the above procedure, the water inside the tank could be well degassed. The idea of this degassing procedure is to create large pressure difference between inside and outside degassing tank, so that the air inside tank will be drawn out of the tank when the top valve is opened. Therefore the air concentration in the tank will significantly decrease. According to the Henry's Law, which is shown in Eq. 3.1, the amount of dissolved air is proportional to the air concentration above water. Decreasing the air concentration can decrease the dissolved air in the water. When the air concentration becomes very low, the pressure inside the tank will be stabilized at the saturation pressure corresponding to the target heating temperature (here is 105 °C). Setting the heating temperature above 100 °C is to ensure a large enough pressure difference to push the air out even its concentration is very low:

$$p = k_H c; \qquad \text{Eqn 3.1}$$

where p is partial pressure of air above water and c is concentration of air that dissolved in the water.

To examine whether the water is well degassed or not, tank pressure at various temperatures are measured. Figure 3-5 shows the measure tank pressure after degassing procedure. From the figure, it can be seen that the tank pressure plot is well matched the saturation temperature of water, which indicates very good degassing is achieved.

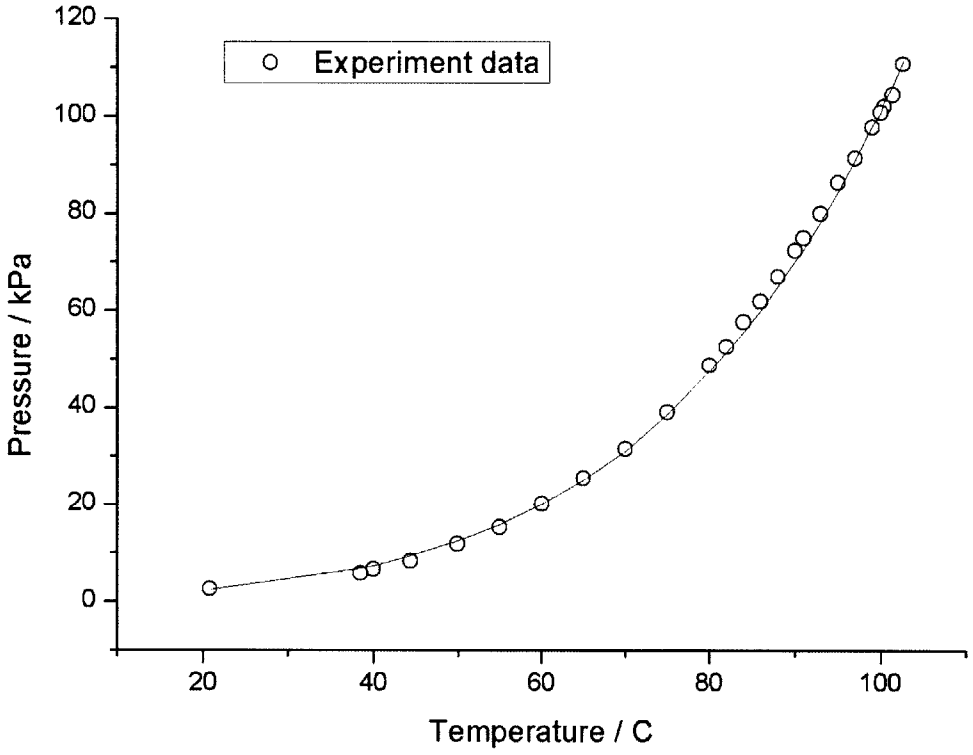

Figure 3-5 Comparison between tank pressure and water saturation temperature in terms of temperature

In order to remove the air inside the loop, a vacuum pump is connected through valve 15. After water is degassed in the degassing tank, the pump is then turned on to remove the air in the rest of loop. Because of the relatively high pressure inside tank, when valve 4 and 10 are

opened, the degassed water will automatically fill the whole loop. After this, the flow loop is ready for running various experiments.

3.3 Inlet Water Temperature Control

In flow boiling experiments, it is very important to have a good inlet temperature control system for various experiments. It is even more crucial for bubble dynamic experiments because it is necessary to heat the water close to a saturation state before it enters into the microchannel, so that it will be much easier to generate bubbles inside the microchannel. In the current flow loop, controlling of the inlet water temperature was achieved by a pre-heater [16], a degassing tank [5], and a post-heater [17], as shown in Figure 3-1. The water was first heated by the pre-heater to about 90°C. Then the water entered the degassing tank, where it was further heated to a target temperature. This was done by placing a thermocouple probe at the outlet port of the degassing tank and using the measured values of the outlet water temperature as an input signal for the On/Off controller. When the exit water temperature was below the target temperature, the controller turned on the power of the Kapton heaters to heat the water inside degassing tank until the exit water temperature reached the target temperature. The water coming out of the tank was transported through a vertical section of pipe before entering the microchannel. A post-heater was installed on the vertical pipe to compensate for any heat lost during the transportation. The temperature of the inlet water into the microchannel was monitored throughout the experiments.

The inlet temperature variation during 20 minutes duration at a flow rate of 132 mL/min is shown in Figure 3-6. As can be seen from the figure, the inlet temperature varied no more than +/-1°C. This temperature oscillation was caused by the on/off control method. However, considering that the operating temperature is around 100°C, and that the period of temperature oscillation was long compared to the bubble nucleation period, this inlet temperature variation was acceptable for boiling experiments.

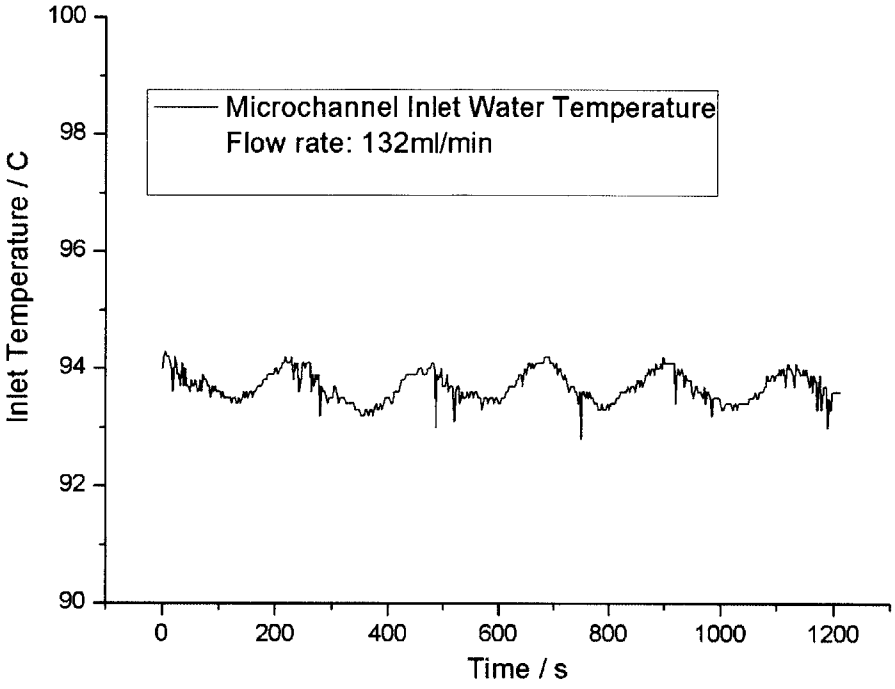

Figure 3-6 Microchannel inlet water temperature variation

3.4 Chapter Summary

In this chapter, a flow loop for various experiments is presented. The loop can provide very good degassing work and fluid temperature control. The whole loop setup was built around an optical microscope, which allows people to observe and record images for experiments.

Chapter 4

Bubble Dynamics in a Microchannel under Flow Boiling Conditions

In order to understand the bubble dynamics on structured surfaces in a microchannel under flow boiling conditions, several experiments are conducted. In this chapter, an experimental setup that allows for observation of the bubble dynamics in a microchannel in a side view and the preliminary results are presented.

4.1 Test Samples: Silicon Micropillar Array Surfaces

The structure surfaces studied in this thesis were silicon micropillar array surfaces. Figure 4-1 shows the SEM pictures of the micropillar array surfaces. Pillars of five different sizes were fabricated. The diameters of the pillars were 5 μm and 10 μm and the spacing (edge to edge) were from 5 μm to 15 μm. All pillars had a height of 20 μm. Table 4.1 shows the details of pillar dimensions and corresponding surface properties. The pillar dimensions were designed to meet the imbibition condition [21], which is a criterion for water to completely wet the surface, as shown in Eq. 4.1:

$$\theta_Y < \theta_C \; with \; cos\theta_C = \frac{1-\varphi}{r-\varphi}; \qquad Eqn\ 4.1$$

where θ_Y is the equilibrium contact angle, φ is the solid fraction and r is the roughness.

Table 4.1 Dimensions of silicon micropillar array surfaces

Device #	Diameter(μm)	Spacing(μm)	Height(μm)	r	φ	θ_c
1	5	15	20	1.785	0.049	56.78
2	5	10	20	2.396	0.087	66.71
3	10	10	20	2.571	0.196	70.21
4	10	5	20	3.793	0.349	79.11
5	5	5	20	4.142	0.196	78.24

Figure 4-2 shows the details of the fabrication procedure. The procedure started with a 6 inch silicon wafer with a 300nm silicon dioxide layer on the surface. A 2 μm thick layer of OCG 825 positive photoresist was first coated onto the silicon surface by spin coating. Then photolithography was used to produce the pillar pattern on the photoresist layer. Next, the silicon wafer underwent a Reactive-ion etching (RIE) to etch through the silicon dioxide layer, which transferred the pillar pattern from the photoresist layer to the silicon dioxide layer. After RIE, the Deep Reactive-Ion Etching (DRIE) was processed to etch the 20 μm high pillars. In this step, the silicon dioxide layer works as a mask, which was good for etching high aspect-ratio structures. After DRIE was the piranha cleaning to remove the photoresist and the wafer was further cleaned by acetone, IPA and DI water. Lastly, the wafers were cut by dice saw into 33mm x 21mm pieces for experiments.

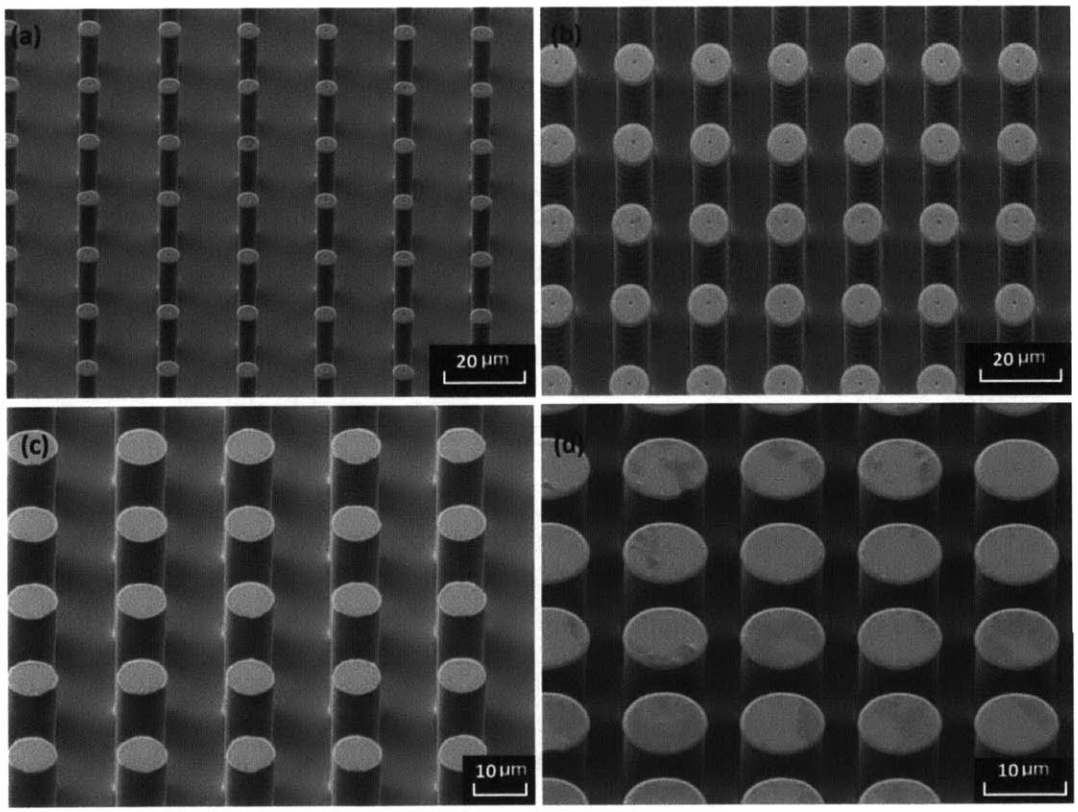

Figure 4-1 SEM images for the silicon micropillar array surfaces. (a) 5 μm diameter and 15 μm spacing; (b) 5 μm diameter and 5 μm spacing (c) 10 μm diameter and 10 μm spacing (d) 10 μm diameter and 5 μm spacing

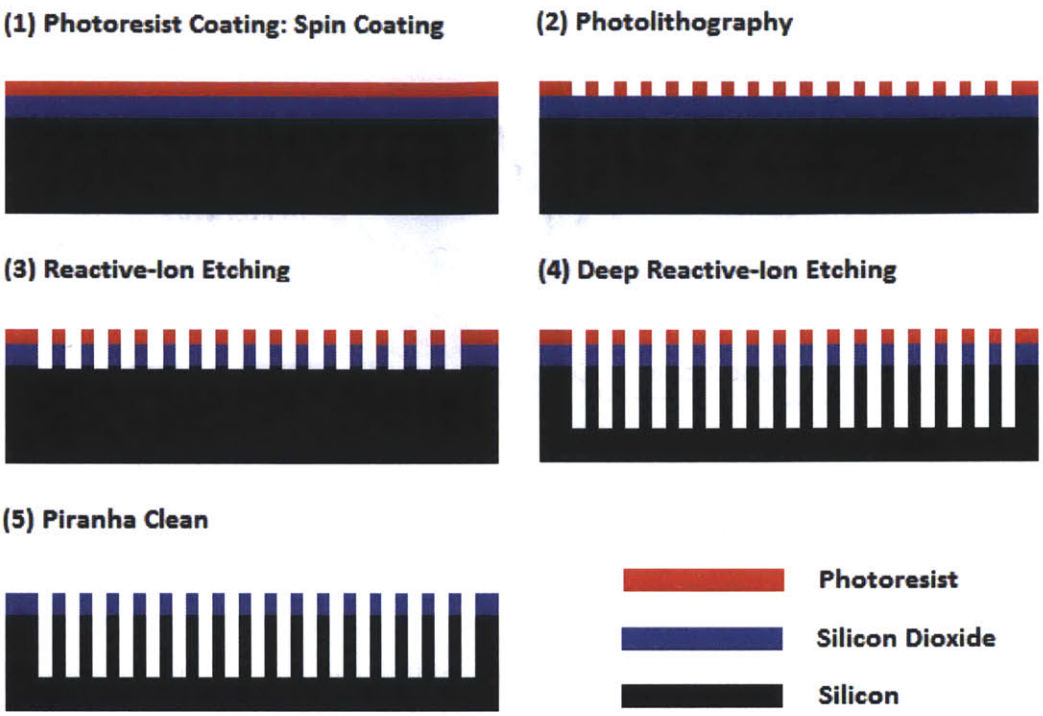

Figure 4-2 Fabrication procedure of silicon micropillar array surface

In flow boiling experiments, a heater is necessary for providing heat flux from the backside of the sample for bubble nucleation. In this thesis, a 6.35 mm wide and 25.4 mm long Kapton heater was used. It bonded to the silicon sample by thermally conductive epoxy. A layer of non-conductive epoxy was then coated on top of the Kapton heater to prevent water from directly contacting the heater, and therefore no bubble would generate at the backside of the heater. Then the silicon sample was bonded to a Teflon block by the same non-conductive epoxy. The epoxy coating cured after 24 hours at 85°C. Then the sample along with the Teflon block was placed into the fixture for experiments. Figure 4-3 shows the layout of the silicon sample with the Kapton heater.

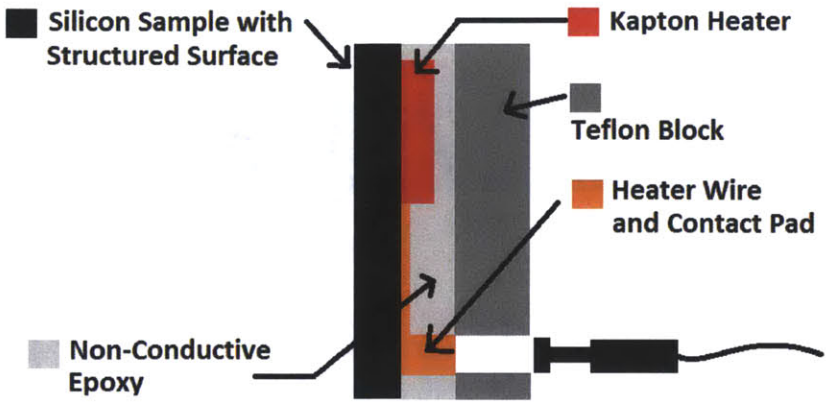

Figure 4-3 Layout of structured silicon sample with Kapton heater

4.2 Test Fixture

A testing fixture was designed for the flow boiling experiment. The design of the flow boiling fixture is shown in Figure 4-4. The fixture consisted of an inlet/outlet port, sample sink where the test sample would be installed and a Pogo pin slot for wire connection of the Kapton heater at backside of the silicon sample. A sandwich style method was used to form the channel by two structured silicon samples and multiply silicon samples with smaller height in between as the spacers. Thus the channel dimension was determined by the number of spacers used. Samples were then placed into the sample sink in the fixture with 2 Teflon blocks, which were used to fix the samples tightly in the fixture. On top of the fixture, a steel clamping plate was used to seal the channel with a Lexan glass providing optical access, which allowed observation of bubble dynamics in the microchannel in a side view. The details of dimension of this test fixture can be found in Appendix B.

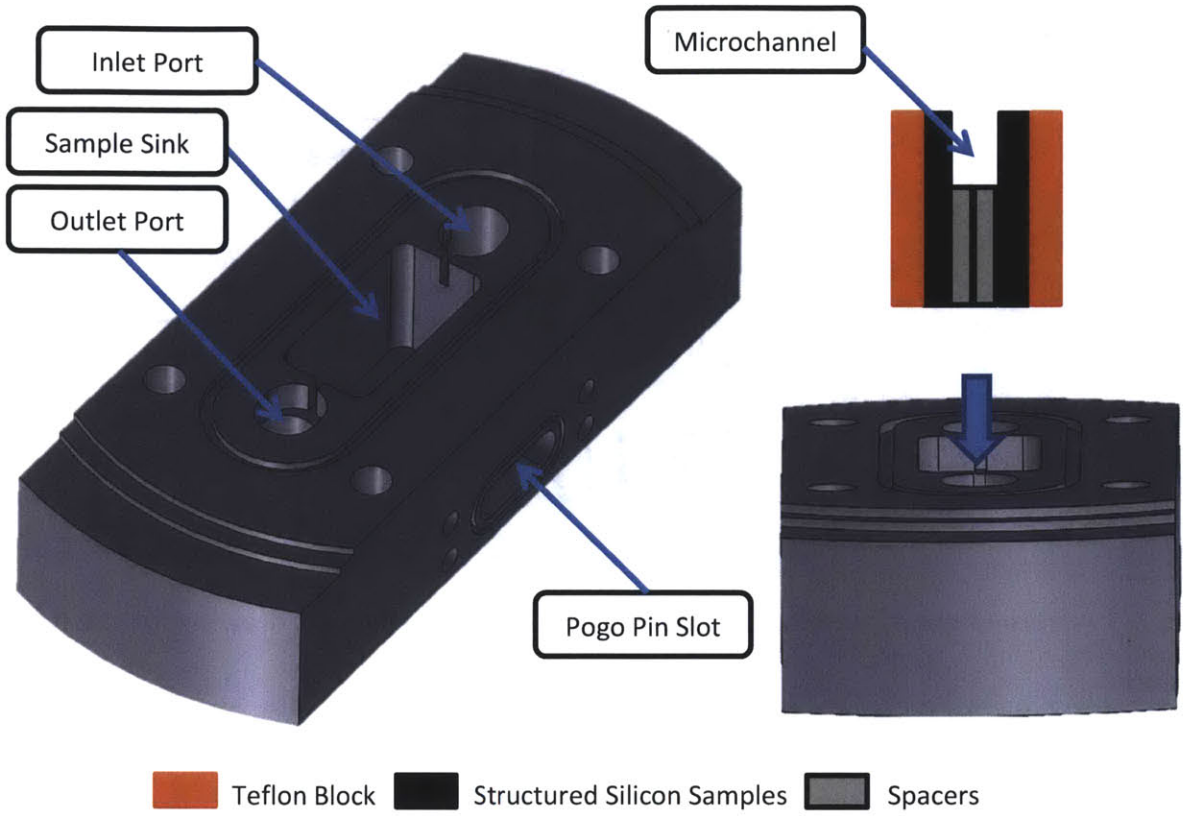

Figure 4-4 Design of the fixture

The whole sample was immersed into the flow environment during the experiment and Pogo pins (HPA-0A, Everett Charles Technologies) were used to connect Kapton heaters at the backside of the sample. In order to have an easy assembly of Pogo pins while keeping the good sealing of the fixture, a special Pogo pin block was designed and manufactured. Figure 4-5 shows the assembled flow boiling fixture and a schematic drawing for the Pogo pin block. Two Pogo pins were fitted on the block. They were permanently sealed by epoxy to prevent air leakage through the fixture. The Pogo pin block was mounted onto the fixture by 4 screws. An O-ring was used to seal the gap between the Pogo pin block and the fixture. This design made it much easier to remove the Pogo pin to change samples in the fixture, and at the same time, the O-ring also provided good vacuum sealing.

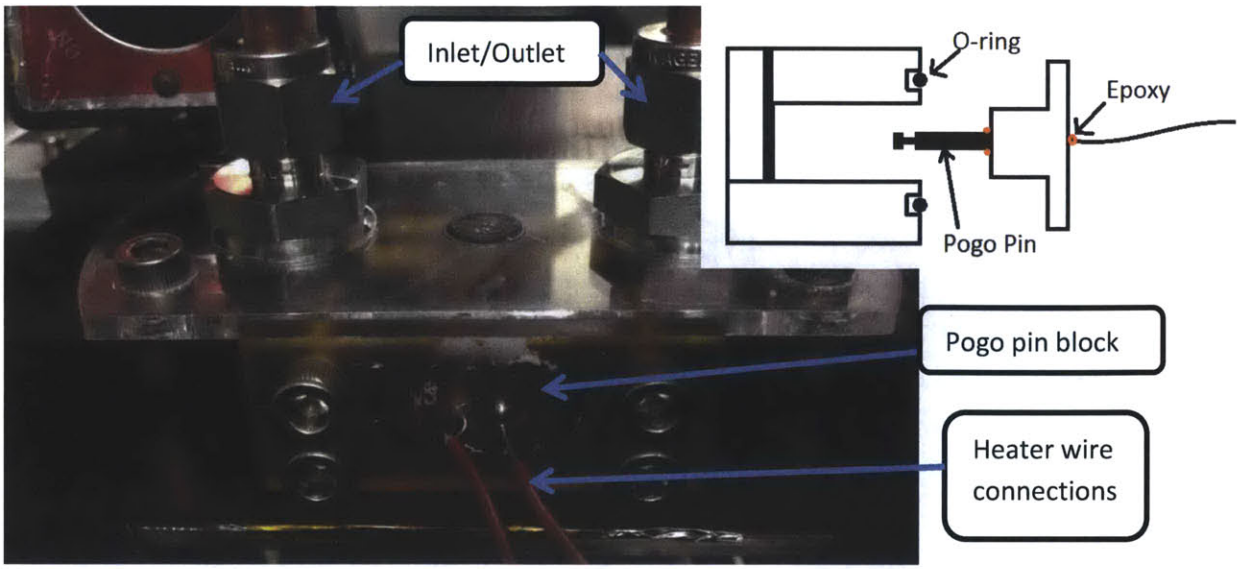

Figure 4-5 Picture of the assembled flow boiling fixture and a schematic drawing for the Pogo pin block.

4.3 Experiment Procedure

To run the flow boiling experiments, we first assembled the fixture with silicon micropillar array surface installed inside and connected it to the flow loop presented in Chapter 3. Then we degassed the water in the degassing tank and pumped air out of the inside loop by vacuum pump. After degassing work, we turned on the peristaltic pump to target flow rate, pre-heater and post heater; set the target inlet temperature to 100 °C and let the loop run for 15 minutes to allow the flow to be stabilized. Then the Kapton heater at the backside of silicon sample was turned on to the desired heating power and the loop was run for another 10minutes. After all conditions were steady, a high-speed camera was turned on to record high-speed video of bubble dynamics in the microchannel.

4.4 Results and Discussion

Firstly, different bubble departure modes were observed during the flow boiling experiments. The most common departure mode that occurred in this experiment was sliding, which was the result of the inertia force that overcame the surface tension force in the flow direction. Figure 4-6 shows a bubble growth and sliding process on the 5μm diameter, 5μm spacing micropillar array surface.

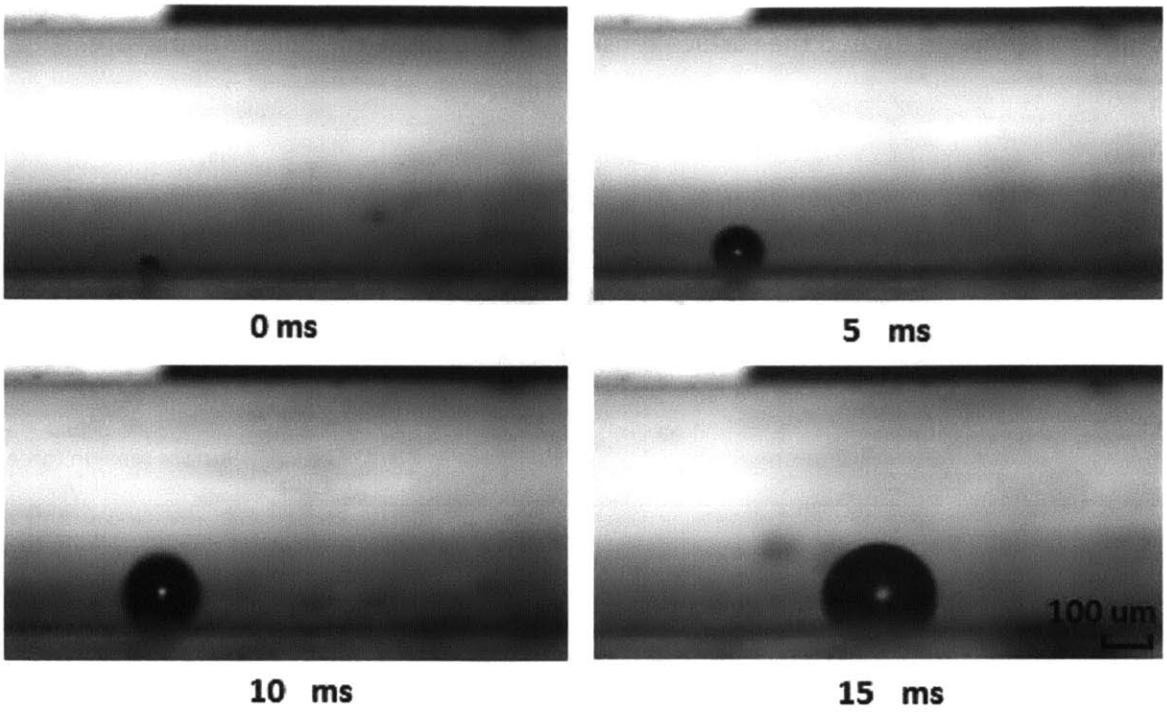

Figure 4-6 Bubble growth and sliding process on 5 μm diameter, 5 μm spacing micropillar array surface. Channel dimension: 0.65 mm in height and 5 mm in width, Flow rate: 307.3 kg/m^{2}s, heat flux: 7.9 W/cm^2.

The second departure mode that was observed was a bubble directly departing from the surface shortly after it nucleated. Figure 4-7 shows a process of this type of bubble departure mode. This departure mode may be caused by the large difference between inside and outside pressure of the bubble. A simple estimation was made to verify whether the pressure difference could generate enough force to cause bubble departure. Assume that a bubble nucleates from a 10 μm cavity with a wall superheat of 20 °C, which corresponds to a saturation pressure of 199 kPa. Assume that the bulk temperature of flow was 100 °C with a pressure of 100 kPa, which leads to a pressure difference of 99kPa. Estimate that the effective area the pressure acts on a bubble to push it to depart from the surface is the same as the area of the cavity, as shown in Figure 4-7-b, which results in a force of 7.9×10^{-6} N. The maximum surface tension force that holds the bubble at the same cavity is about 1.8×10^{-6} N, which is smaller than the pressure estimated above. More accurate calculation is needed to obtain the force generated by the pressure difference; however, the same magnitude of estimated values

of pressure and surface tension force indicates that it is possible for force generated by pressure difference to exceed the surface tension force to cause the bubble departure.

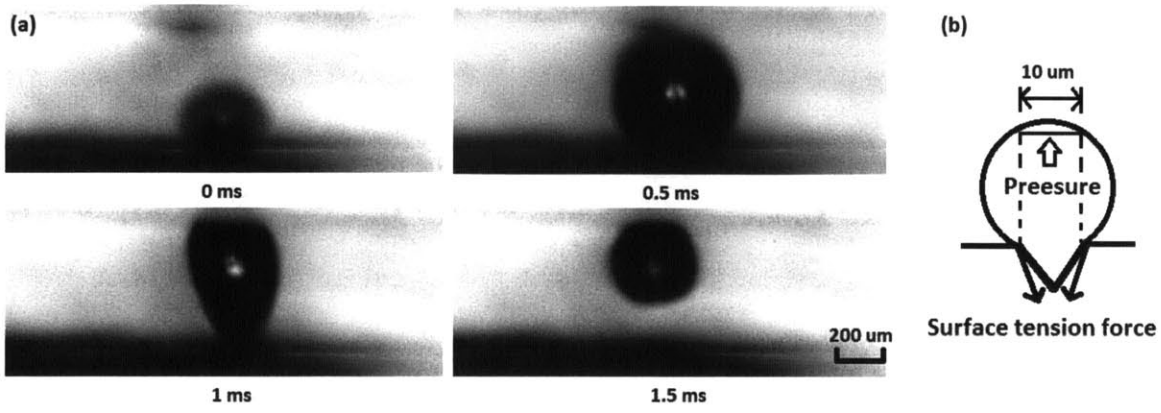

Figure 4-7 (a) Bubble growth and direct departing process on plain surface. Flow rate: 307.7kg/m^{2}s; Heat flux: 7.9W/cm^2. (b) Schematic diagram of estimated effective area the pressure acts on to cause bubble departure from the surface.

The third bubble departure mode was bubble interaction. Under low heat flux condition and on an inefficient bubble removal surface, the nucleated bubbles could interact with each other. Two bubbles may merge into one bubble and the released surface energy could be high enough to push a bubble to jump away from the surface. Figure 4-8-a shows a process by which two bubbles nucleated on surface, interacted with each other and departed from surface. Figure 4-8-b shows a process that one bubble nucleated on surface, interacted with a departed bubble from upstream and then departed from the surface. Bubble interaction seemed to be an efficient way to remove the bubble from surfaces, enhancing the bubble merging or other interactions potentially could be another direction to improve the bubble departure.

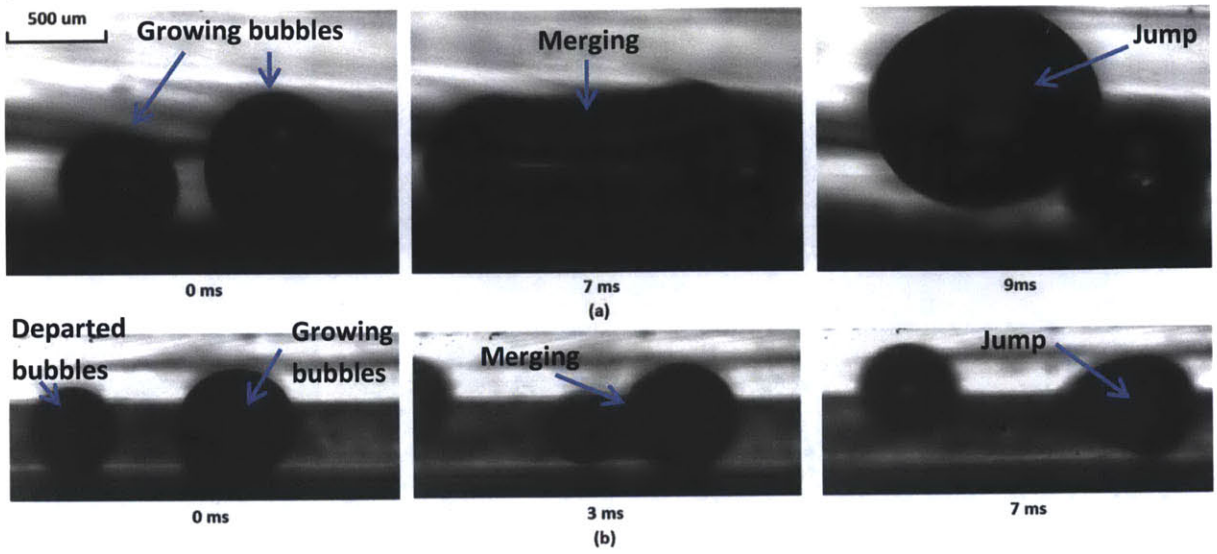

Figure 4-8 Bubble departure process due to the bubble interactions (a) Two bubbles merged and departed from surface (b) One bubble merged with a departed bubble and depart

The fourth mode that has been observed in experiments was oscillating departure. When a bubble just nucleates on a superheated surface, the temperature of the bubble is believed to be same as the wall temperature. If there exists inlet liquid subcooling, the bubble will lose heat to the subcooled liquid. The rate of heat loss will increase with the increasing of the bubble size until it reaches a maximum size. At that time, the bubble loses more heat than it obtains from the superheated wall. As a consequence, its size will start to decrease until more heat energy is input into the bubble. Therefore, an oscillation forms and the amplitude will increase with time. In some conditions, the oscillation could be large enough to pull the bubble away from the surface, which leads to a bubble departure. Figure 4-9 shows a bubble departure process due to the bubble oscillation on plain surface.

It was also found that different departure modes may coexist on the same surface. This was probably caused by the non-uniform heating condition and different cavities where bubbles nucleate.

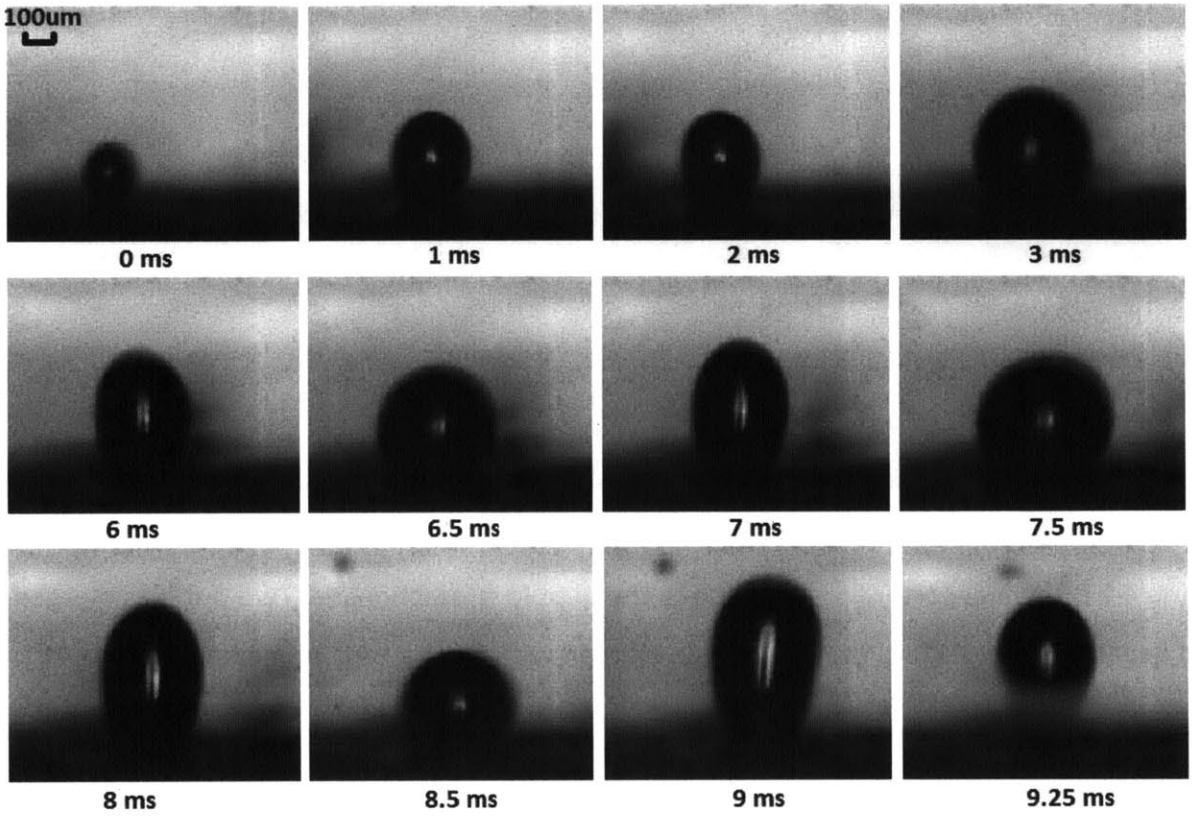

Figure 4-9 Bubble departure process on plain surface due to the bubble oscillation. Flow rate Flow rate: 307.3kg/m^{2}s, heat flux: 7.9W/cm^2

Next, the bubble departure sizes at various flow rates of different departure modes were measured. A direct departing mode was observed on a plain surface in a 5 mm wide and 0.65 mm high microchannel. The measured bubble departure radius as a function of flow rate is plotted in Figure 4-10. From the figure, it can be seen that the departure radius is independent of flow rate. The potential explanation for this trend is that for this type of departure mode, the pressure difference between inside and outside a bubble determines whether the bubble will depart or not, rather than flow inertia force. Therefore, wall superheat may be more important because it determines the pressure inside a bubble when it just nucleates. A sliding departure mode was found on a 5μm diameter, 5μm spacing pillar array surface and the measured departure radius in terms of flow rate is also plotted in Figure 4-10. As can be seen, the departure radius decreases with increasing of the flow rate. This is because the flow inertia is the dominate force to cause the bubble sliding.

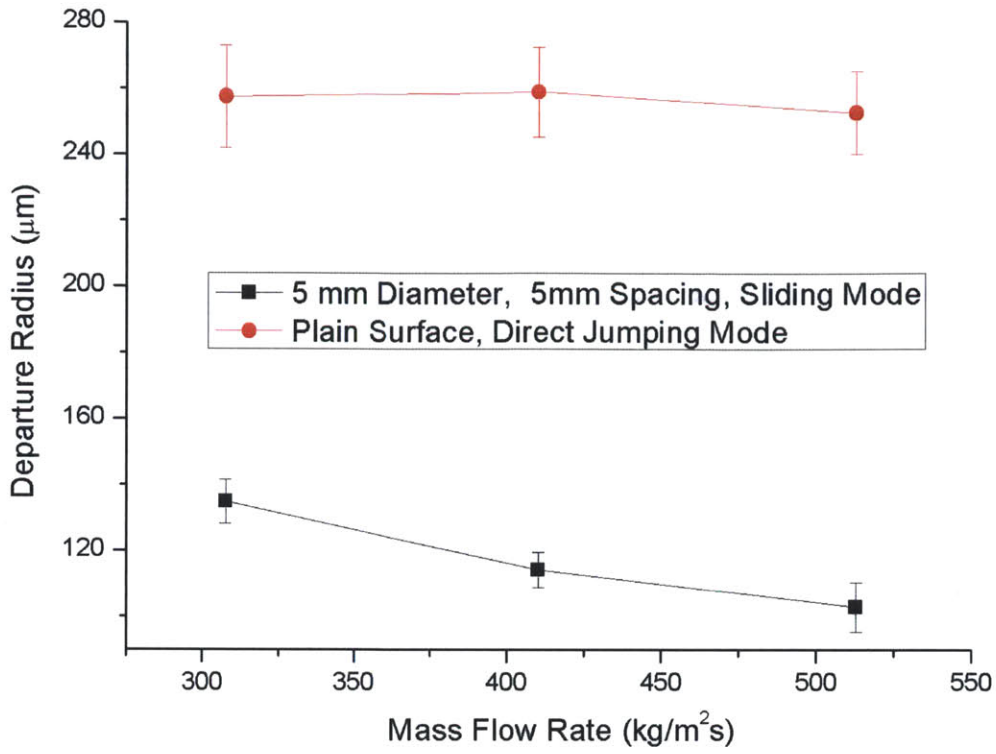

Figure 4-10 Departure radius in terms of mass flow rate under flow boiling condition. Channel dimensions: 0.65mm in height and 5mm in width.

The observed departed bubbles were believed to nucleate on the defects of the surfaces and these observed departure process may give certain information about the bubble departure behaviors on micropillar array surfaces under flow boiling conditions. However, the problem was that the nucleation was not controllable. The nucleation conditions might differ from surface to surface and the departure modes might also be different. It can be learned from Figure 4-10 that different departure modes may have different departure behaviors. Therefore, without well controlled bubble nucleation sites, it will be very difficult to compare experiment results and understand how surface structures affect bubble dynamics.

In order to obtain better understanding of the effects of surface structures on bubble dynamics under flow boiling condition, it is critical to create nucleation sites on structured surfaces. Several attempts were made to create a single nucleation site on micropillar array surfaces in this thesis. One idea is to change the surface property of a small area from hydrophilic to hydrophobic. This area needs to be small enough, ideally 10 μm to 50 μm, that it

will not affect bubble departure behavior. First, an attempt was made to drop 1-5 10 μm droplets of Teflon solution by inkjet printing to create a small hydrophobic spot on a structured surface. However, the Teflon solution was so viscous that it was difficult to jet a single 10 μm droplet of solution. It had to accumulate a certain number of droplets until the gravity force is large enough to pull the droplet down from the inkjet nozzle. The final size of the hydrophobic spot created by inkjet printing of Teflon solution was larger than 1mm, which was not good for bubble dynamics observation experiments.

Another attempt was made by using a 5 μm glass tip covered with uncured Epoxy to contaminate a small area of the structured surface. With precise control of the tip movement, small dots of Epoxy were successfully dropped onto the surface. Further tests need to be done to prove that these Epoxy dots can work as nucleate sites and will survive during the flow boiling experiments.

Drilling a small hole on a surface is also possible to create a single nucleation site. In this thesis, attempts were made to create 10 μm to 30 μm rectangle holes with depths of 10-30 μm by Focused Ion Beam (FIB) on structured surface. Figure 4-11 shows a 10 μm hole with a 10 μm depth created by FIB on micropillar array surfaces. However, the experimental results show that these holes do not work as nucleation sites. The possible reason was that shape of hole is also important to determine whether it could trap air and work as a nucleation site. Potential improvement for this method is to create an even higher aspect ratio hole (for example, 20 μm wide and 100 μm deep hole), so it could trap the air more effectively. Further tests needs to be done to verify this method.

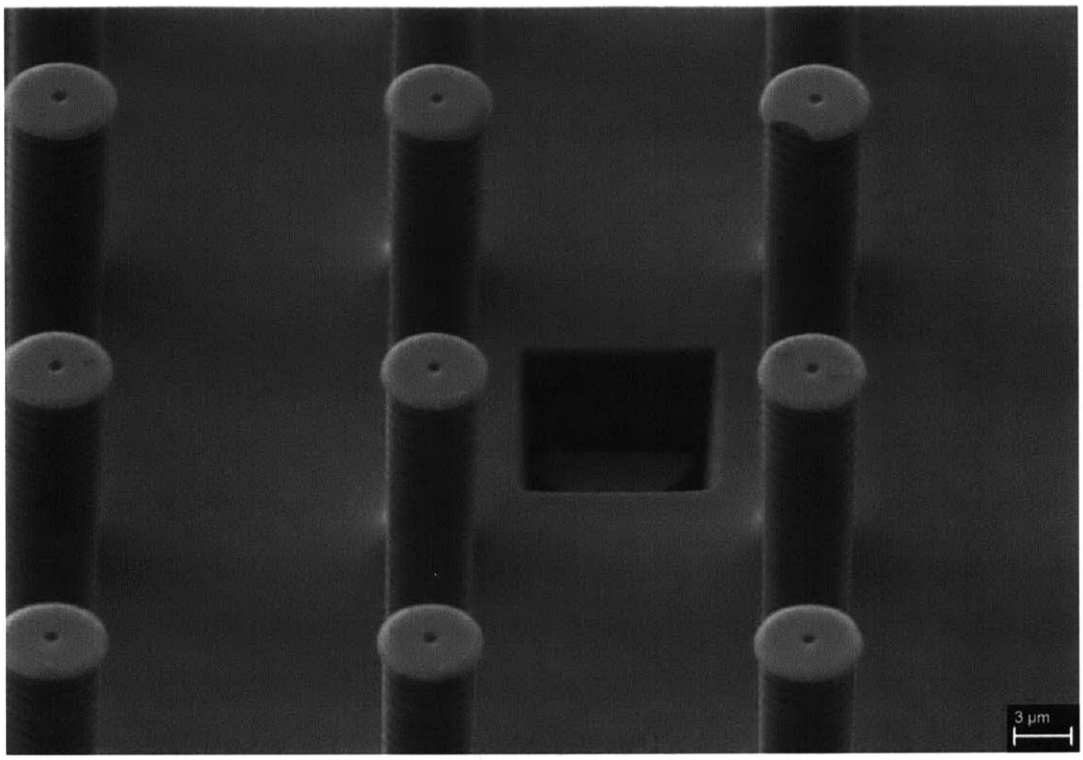

Figure 4-11 10 µm wide, 10 µm deep hole created by FIB on 5 µm diameter, 15 µm spacing micropillar array surface.

4.5 Discussions of Advantages of Micropillar Array Surfaces

The experimental results have shown that a pillar array surface may not be the ideal surface for bubble nucleation, which may bring high wall superheat and cause flow instability due to the rapid expanding bubbles that nucleate at high temperature. So the question is why it is still interest in for flow boiling. When it comes to the flow boiling performance, two factors are usually considered: one is the heat transfer coefficient, which indicates how effectively it removes the heat; the other one is CHF, which indicates the maximum heat it can dissipate through this cooling method. The micropillar array surface is potentially able to improve the flow boiling performance on both directions.

In terms of considering the heat transfer coefficient, pillar array could introduce a great number of liquid films between the pillars, which would bring a lot of thin film evaporation. Research studies have shown that thin film evaporation has an extremely high heat transfer coefficient, and thus it could help to improve the heat transfer coefficient of flow boiling.

In CHF consideration, with proper design (high solid fraction to form Cassie bubble), the pillar array surface could maintain a liquid layer within structures under bubbles, which could prevent early drying out of liquid film to cause the CHF.

The pillar array surfaces are also possible to stabilize the flow. The departed bubble may retouch the heated surface downstream, which has been observed in experiments. For the plain surface, when a bubble retouches the surface, it will experience a second growing process. If a pinning just happens at that place, the regrown bubble is more likely to grow into a vapor slug and block the whole channel, which potentially could cause the flow instability. Figure 4-12-a shows this bubble regrowth process on the plain surface. However, for the micropillar array surfaces, the modeling work in Chapter 2 has predicted that the bubble will not grow downwards into the structures when it starts from the top of pillars. So if the bubble retouches the heated surface, it will stay on the top surface of pillars. Usually, it has low a heat transfer coefficient at the top surface of pillars, thus the bubble regrowth process will be much slower. At the same time, because of having less contact area with surface, the bubble is also easier to remove. Therefore even if the bubble retouches the top surface of pillars and experiences a regrowth process, it will not cause significant change of the system. Figure 4-12-b shows a bubble retouch process on a micropillar array surface. Although it might not dissipate more heat from this retouch process, it was helpful to keep system stable and eventually might improve the CHF.

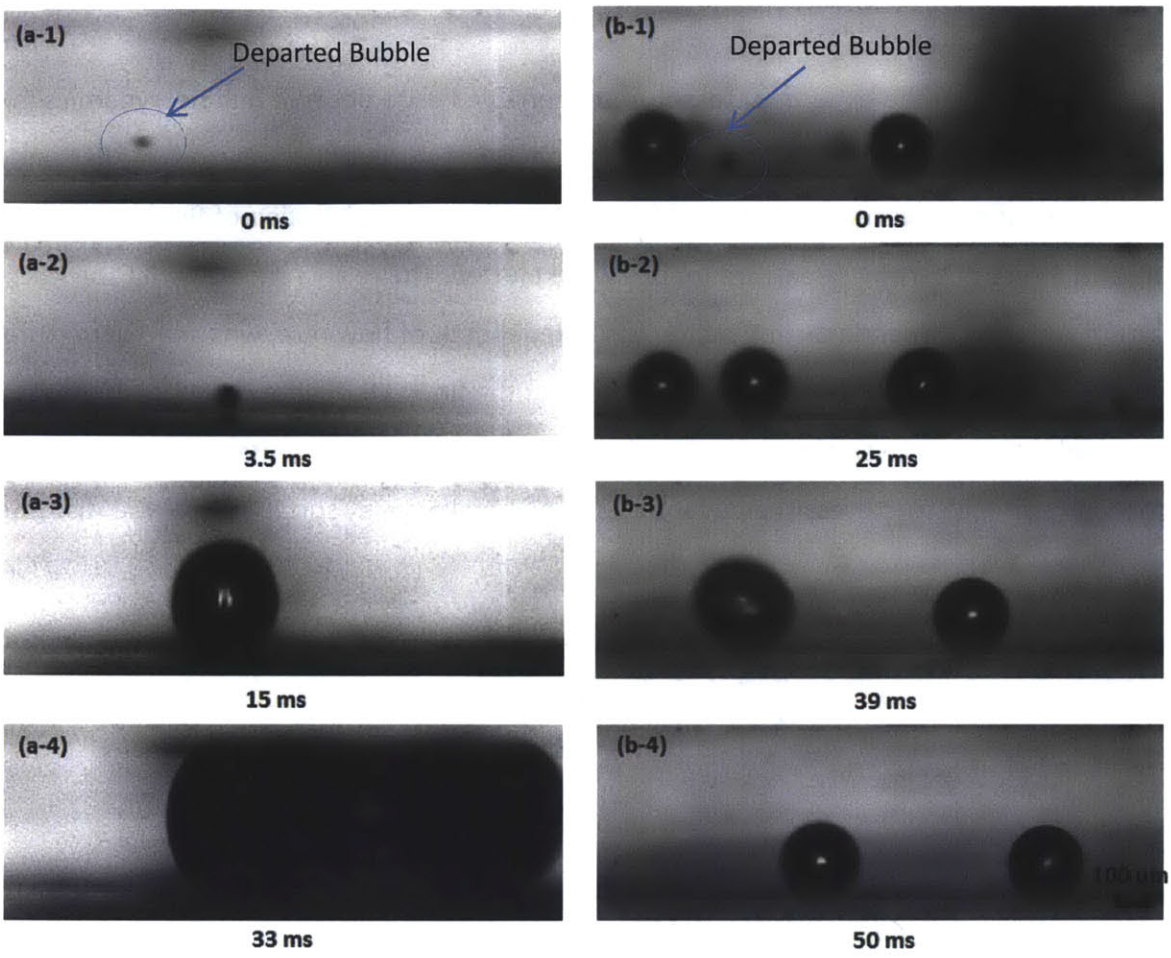

Figure 4-12 Bubble regrowth process on plain surface and structured surface. (a) The bubble retouched the heat surface and grew into a slug on plain surface. (b) The bubble retouched the heated surface and experienced a slower regrowth process on a 5 μm diameter, 5 μm spacing silicon pillar array surface.

Ideally, the pillar array surface with proper nucleation sites design is desired for flow boiling in microchannels. It is able not only to provide good bubble nucleation sites, but also able to maintain a high heat transfer coefficient at high heat flux, as predicted. Although more work needs to be done on this type of structured surface, it has already shown the potential ability to improve the performance of flow boiling in microchannels.

4.6 Chapter Summary

In this chapter, an experimental setup that enabled us to observe bubble dynamics in microchannels under flow boiling conditions is presented. Four bubble departure modes under flow boiling condition were identified. Bubble departure radii as a function of flow rates of sliding and direct departing departure modes were plotted. The results showed that the departure radius of direct departing mode was independent of flow rate, while the departure radius of sliding mode decreases with the increase of the flow rate. Three potential methods were presented to create single nucleation site on surfaces for better understanding the functions of surface structures. The advantages of micropillar array surface were also discussed in this chapter.

Chapter 5

Bubble Departure on Structured Silicon Surface by Air Injection

As it is difficult to create a single nucleation site on a structured surface, a new method is put forward to create a single bubble on a structured surface without any heating. That is injecting air from the backside of a silicon sample. Since the bubble departure in a microchannel is dominated by surface tension force and inertia force, observing the bubble created by air injection still could give useful information about the bubble departure behavior on a structured surface. In this chapter, an experiment to study the bubble departure on silicon micropillar array surfaces by air injection is presented.

5.1 Test Sample

The test samples used in this experiment were the same silicon micropillar array silicon surfaces that were used in the flow boiling experiments in Chapter 4. In order to inject air from the backside, an additional hole through the silicon sample is required. The size of the hole needs to be small enough so that it will not affect the bubble departure on micropillar array surfaces. The tool used to create the small hole for injection was a laser cutter. By precise controlling the number of laser pulses shooting on the surface, mouths varying from 10 μm to 40 μm were achieved on the pillar array side, which were very close to the required cavity size for bubble nucleation under boiling condition. Figure 5-1 shows the microscope images of laser holes on micropillar array surfaces.

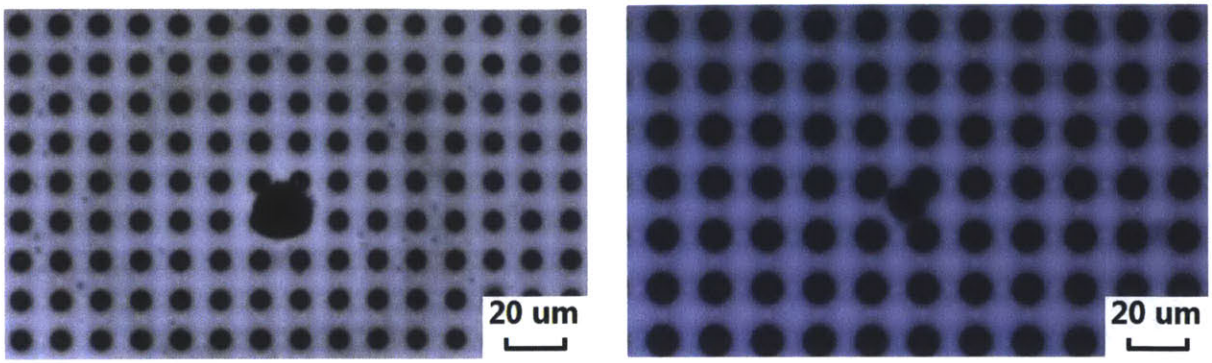

(a) (b)

Figure 5-1 Microscope images of laser holes on micropillar array surfaces. (a) 5 μm diameter and 10 μm spacing pillar arrays (b) 10 μm diameter and 10 μm spacing pillar arrays

5.2 Test Fixture

Figure 4-2 shows the design of the test fixture for the experiment of single bubble dynamics observation by air injection. The fixture was made of Ultem1000 and machined by a Computer Numerical Control (CNC) micro milling machine.

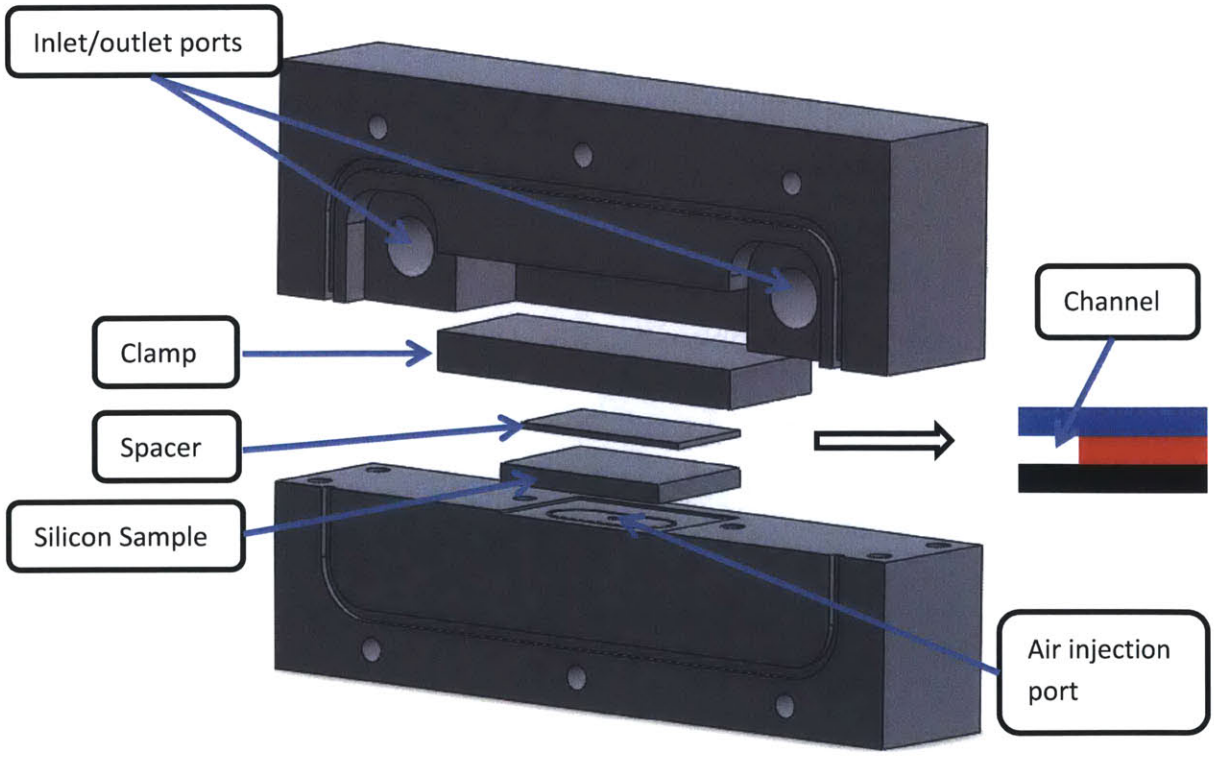

Figure 5-2 Design of the fixture for bubble dynamics observation by air injection

As can be seen from Figure 5-2, the fixture consisted of two parts. The test samples were placed on the bottom part of fixture and a hole was drilled beneath the sample, through which air was injected onto the structured surface. The backside of the silicon sample was sealed with an O-ring to prevent air leakage. On the silicon sample was the spacer, which is 5mm shorter in width. This determines the size of the channel. In this experiment, 2 pieces of silicon samples were used as a spacer (33mm in length, 16mm in width and 0.65mm in thickness). Therefore the microchannel in this study was 33mm long, 5mm wide and 1.3mm high. The spacer and structured silicon sample were fixed on the bottom part of the fixture by a clamp. The inlet and outlet ports were on the upper part. The two parts of the fixture were bonded together by 2 screws and sealed by an O-ring to prevent water leakage. The side of the fixture was covered by a piece of Lexan glass, which provided an optical path for observing the bubble dynamics in a side view. The assembled fixture with silicon micropillar array surface inside is shown in Figure 5-3.

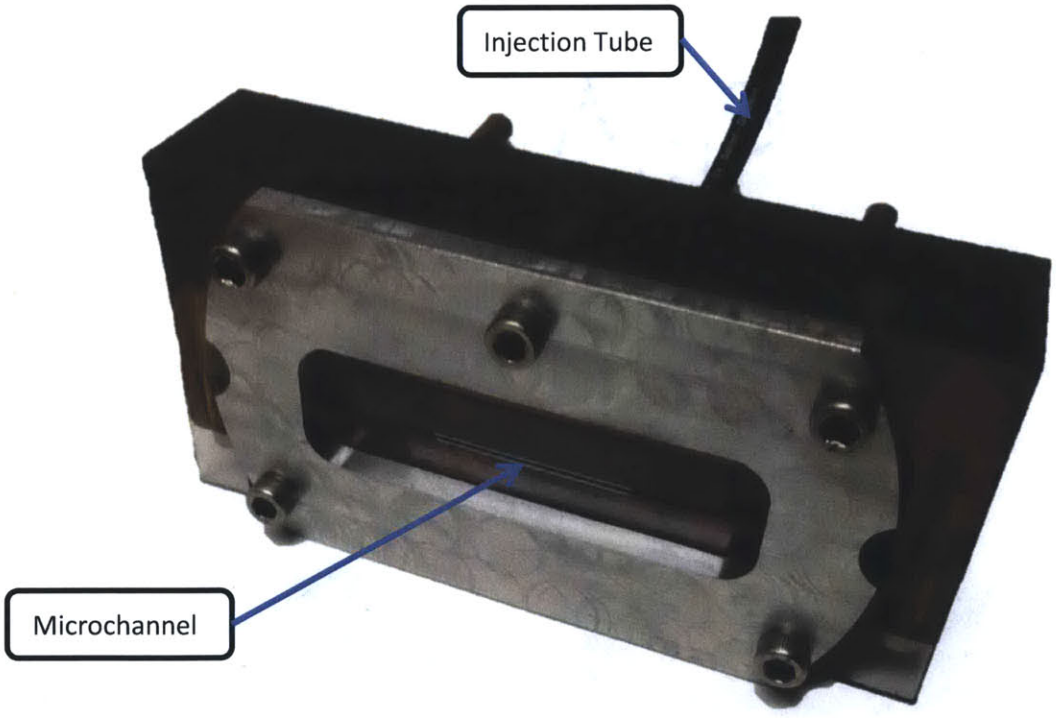

Figure 5-3 Assembled test fixture for bubble dynamics observation by air injection

5.3 Experimental Procedures

To run the experiments, the assembled fixture was first connected into the flow loop as discussed in Chapter 3 and the fixture was placed on the inverted microscope with the side of the microchannel facing the micro lens. Then the peristaltic pump was turned on and the flow rate was adjusted to the desired value. The loop was run for 10min until the flow rate become stable. After the flow was stable, air was injected into the channel through the injection tube and high speed videos of bubble dynamics were recorded by Phantom v 7.1.

5.4 Results and Discussions

A typical bubble growth and departure process is shown in Figure 5-4. It was a bubble growth and departure process on a 10 μm diameter and 10 μm spacing pillar array surface. The flow rate was 153.8 kg/m^{2}s.

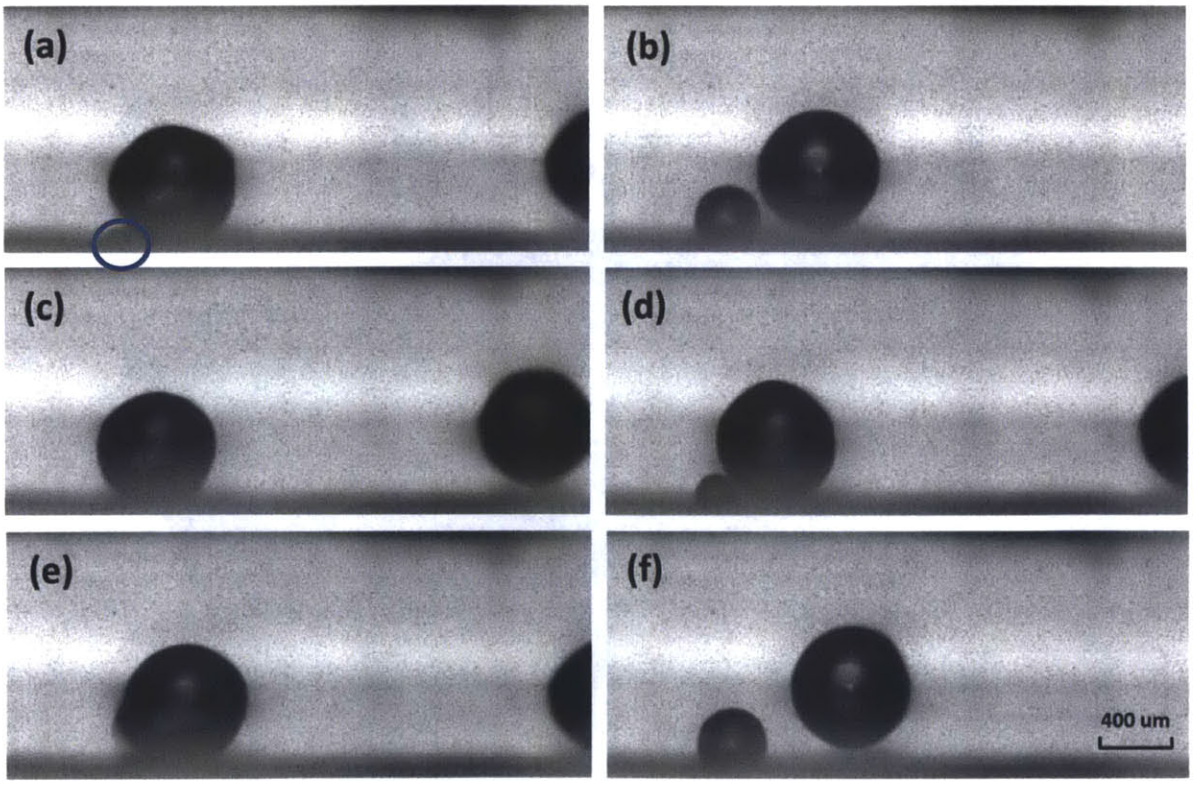

Figure 5-4 Bubble growth and departure process on 10 μm diameter and 10 μm spacing pillar array silicon surface under flow rate of 153.8 kg/m^{2}s.

The bubble started to grow after the previous bubble departed from the surface (Figure 5-4-a). It kept growing (Figure 5-4-b) until it reached the size such that inertia force was large enough to overcome the surface tension force. It then started to slide on the surface (Figure 5-4-c) and leave a space for another bubble to grow (Figure 5-4-d). In low flow rate, the sliding bubble would not go very far when the new bubble started to grow. They would interact with each other and merge (Figure 5-4-e). A certain amount of surface energy was released during the merging process and transformed into the kinetic energy of merged bubble, which allowed bubble jumping from the surface (Figure 5-4-f).

It needs to be mentioned that in real flow boiling condition, merging with bubble that nucleates at the same place is difficult, because when a bubble departs from where it nucleates, it will take a lot of heat due to the phase change. The surface temperature will go down and need a period of time to reach the required wall superheat to have another bubble nucleation. Usually, during the reheating period, the previous bubble will go far enough that there is no chance for the new nucleated bubble to interact with it. Although the actual departure process may not be exactly the same as what has been observed above, it showed that sliding was the first step of departure if the bubble was not interacting with other bubbles. This was reasonable because in a microchannel system, the bubble departure process is the result of inertia force overcoming the surface tension force and the inertia force in lateral direction is much higher than vertical direction; therefore, it is much easier for the bubble to slide first than jump away from the surface

In order to study the bubble departure behaviors on pillar array surfaces, high-speed videos of the bubble departure process on different structured surfaces at various flow rates were recorded. The departure radius, the radius of a bubble that just departs (sliding or jumping away from the surface) was measured based on the high-speed video. The method used to measure the departure radius was first picking up a frame from the high-speed video of a bubble just departed from surface, then choosing 12 points on the outline of the selected bubble and using the Least Square Fitting method to find a best fit circle for the bubble. The radius of that circle was the measured departure radius. Figure 5-5 shows the frames of bubble

departure on different structured surfaces and corresponding best fit circles under a flow rate of 128.6 kg/m^{2}s.

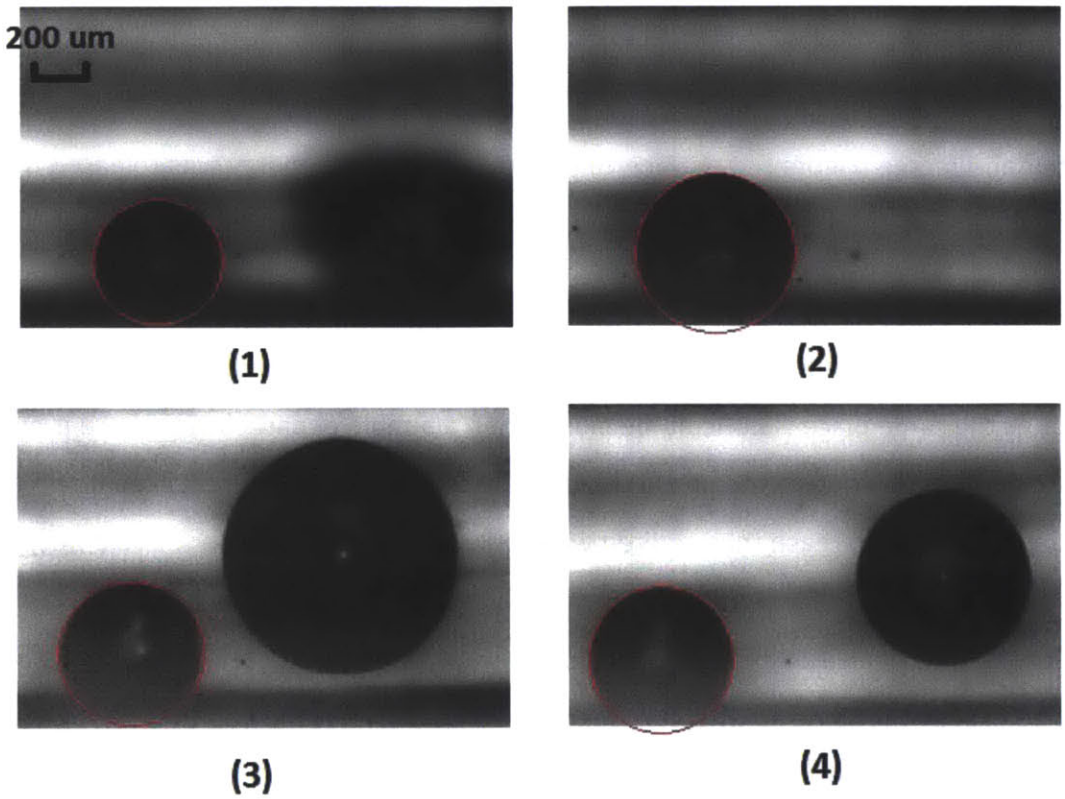

Figure 5-5 Frames of bubble departure on different structured surfaces and corresponding best fit circles under a flow rate of 128.6 kg/m^{2}s. (1) Plain surface (2) 5μm diameter and 15μm spacing (3) 5μm diameter and 5μm spacing (4) 10μm diameter and 10μm spacing

The departure radius in terms of flow rates for different micropillar array surfaces is shown in Figure 5-6. From the figure, it can be seen, as expected, that the departure radii decreased with the increase of the flow rate. Higher flow rate brought larger inertia force, thus leading to smaller bubble departure radii. It also can be noticed that for two 5 μm diameter, 5 μm spacing silicon surfaces with different injection holes in shapes and sizes (one has about 20 μm injection hole and the other one has about 40 μm injection hole), the departure diameter plots followed a similar trend, which indicated that the injection hole had a small influence on bubble departure. This was because the injection holes were relatively small compared to the bubble departure sizes, so most of the surface tension force came from the

interaction between the bubbles and the pillars. Therefore, it is reasonable to directly compare the bubble departure sizes among different micropillar array surfaces to determine which surface makes it much easier for a bubble to depart.

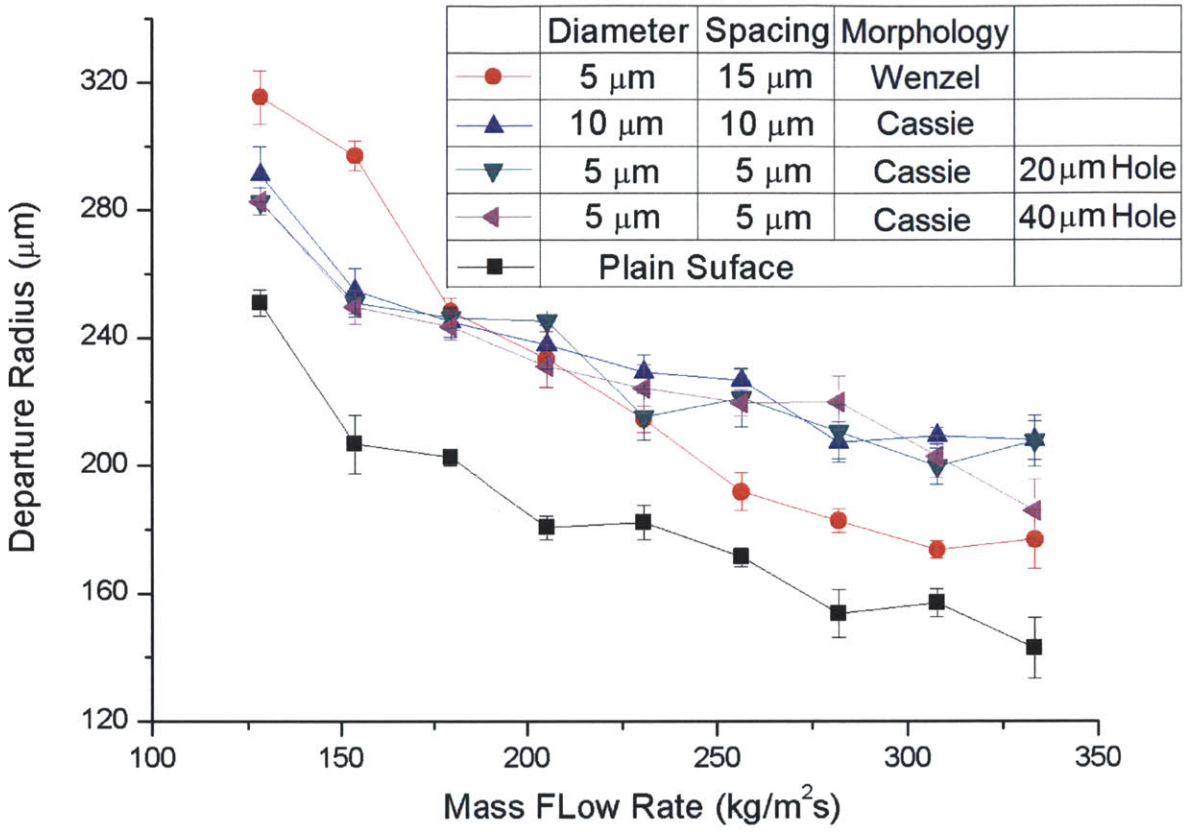

Figure 5-6 Departure radii in terms of mass flow rate for different silicon micropillar array surfaces and plain silicon surface

By comparing the bubble departure size among various surfaces, it can be found that the departure sizes on the plain surface are smaller than those on other micropillar array surfaces. This is because structured surfaces have much higher roughness than the plain surface, which creates more surface tension force to prevent a bubble from departing from the surface.

For the 5 μm diameter, 15 μm spacing surface, it had larger bubble departure sizes in low flow rate than that of the 5 μm diameter, 5 μm spacing and the 10 μm diameter, 10 μm spacing surface. In high flow rate, however, it had smaller bubble departure sizes. This

phenomenon can be explained by the bubble morphology discussed in Chapter 2. For 5 μm diameter, 15 μm spacing surface, the solid fraction is 0.049, which is smaller than the critical solid fraction 0.162. As predicted, a Wenzel bubble will form and the vapor will fill the pillar units at the base of the bubble. On the other hand, for the 5 μm diameter, 5 μm spacing and the 10 μm diameter, 10 μm spacing surface, the solid fraction is 0.196, which is higher than the critical solid fraction. According to the modeling work in Chapter2, a Cassie bubble will form. Since the bubbles nucleate from the bottom of the pillars, more accurately, a Cassie-Wenzel mix state will be maintained, as shown in Figure 5-7-a. As the bubble grows larger, the liquid-vapor interface may touch the top surface of the second pillar (Figure 5-7-b). As long as the interface reaches the second pillar, the vapor will cover its top surface because it leads to a lower energy state. Eq. 5.1 shows the energy change for vapor to cover the top surface of second pillar and clearly, it has a negative value.

$$\Delta E = \frac{\pi}{4} d^2(\gamma_{SV} - \gamma_{SL} - \gamma_{LV}) = \frac{\pi}{4} d^2 \left(\frac{\gamma_{SV} - \gamma_{SL}}{\gamma_{LV}} - 1\right) = \frac{\pi}{4} d^2(Cos\theta_Y - 1). \qquad (Eqn\ 5.1)$$

After the vapor covers the top surface of second pillar, the interface between the first pillar and the second pillar will reshape (Figure 5-7-c). With the bubble keeps growing, the interface may reach the third pillar and start to cover the third pillar. According to the modeling work that has been done in Chapter 2, the interface between pillars will pin at the top of pillars. However, under flow condition, external forces, such as flow inertia and pressure fluctuation, may break this pinning and cause the liquid-vapor interface to move downwards to fill the pillar unit. This pillar unit cell filling process will slow down with increase of the bubble size because of more surface tension will be created due to the larger pillar coverage.

In higher flow rates than 250 kg/m^{2}s, corresponding to the small bubble departure size, the base area, where pillar units are filled with vapor, is still relatively large for high solid fraction surface (5 μm diameter, 5 μm spacing and 10 μm diameter, 10 μm spacing surface) due to the low resistance to prevent the interface from going downwards. In this case, larger surface tension force is created due to the high roughness, which leads to larger bubble departure size. As bubble size increases (in lower flow rates than 150 kg/m^{2}s), the base area

does not grow as fast as bubble itself, which brings smaller increments in surface tension force. However, for low solid fraction surface, on which, Wenzel bubble forms, the base area increases as fast as bubble growing, which results in larger bubble departure sizes in low flow rate. It also needs to be mentioned that since the actual interface evolutions were not observed during the experiments, more evidence is required to prove the above agreements.

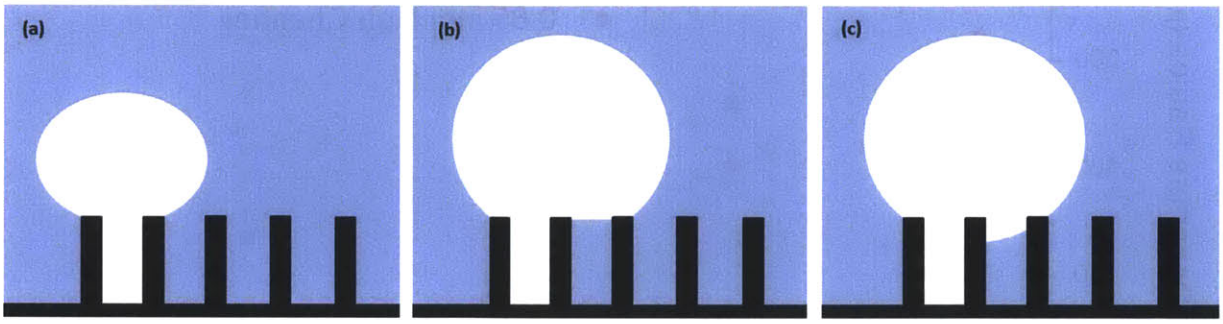

Figure 5-7 Liquid-vapor interface growing process on micropillar array surface with high solid fraction.

Next, the channel size effect was studied. One silicon spacer was removed to reduce the channel height to 0.65mm. The bubble departure radii on 5 μm diameter, 15 μm spacing surface at various flow rates were then measured. The comparison of bubble departure sizes between 1.3mm high channel and 0.65mm high channel is shown in Figure 5-8.

From the figure, it can be seen that the departure radii are smaller in the 0.65mm high channel than those in 1.3mm high channel at the same mass flow rate. This is because in the 1.3 mm high channel, the bubble size was relatively smaller compare to the channel size, and thus the average velocity of flow that impacts the bubble was smaller even though the bulk velocities are the same.

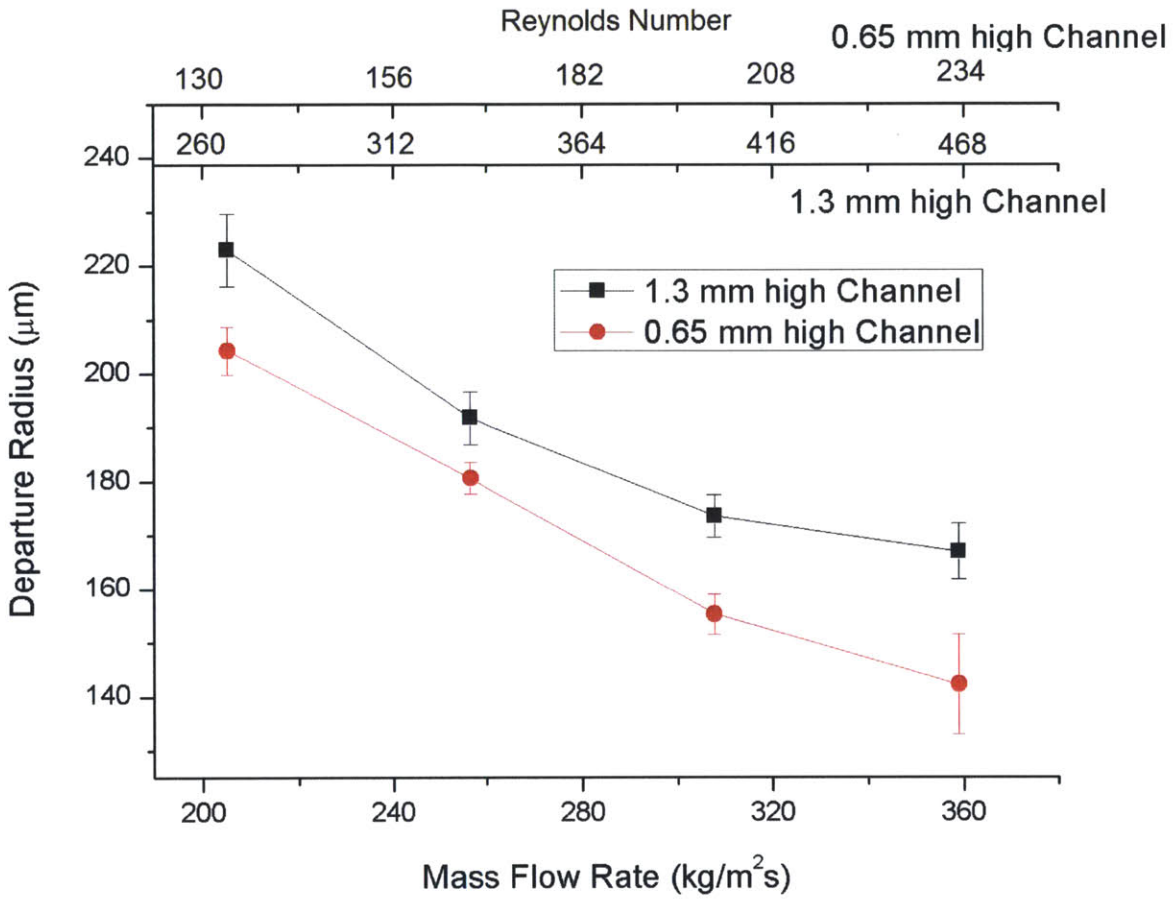

Figure 5-8 Comparison of bubble departure radii on 5 μm diameter, 15 μm spacing pillar array surface between 1.3 mm and 0.65 mm high channels

In order to verify whether the results from the injection experiment are useful for understanding the bubble departure behavior under flow boiling condition, the comparison between bubble departure radius by injection experiment and flow boiling experiment on 5μm diameter, 5μm spacing pillar array silicon surface has been done. The experiments were run in a 33mm long, 5mm wide and 0.65mm high channel and the flow rate ranged from 307.7kg/m^{2}s to 512.8kg/m^{2}s. Figure 5-8 shows the bubble departure radiuses in terms of flow rate by these two types of experiments. From the figure, it can be seen that the departure radii were very close by two experiments at different flow rates. Although not many data points were obtained during the experiments, this preliminary result may indicate the bubble departure characteristics on pillar array surface that obtained by injection experiments is helpful to

understand bubble departure behavior on micropillar array surfaces under flow boiling condition.

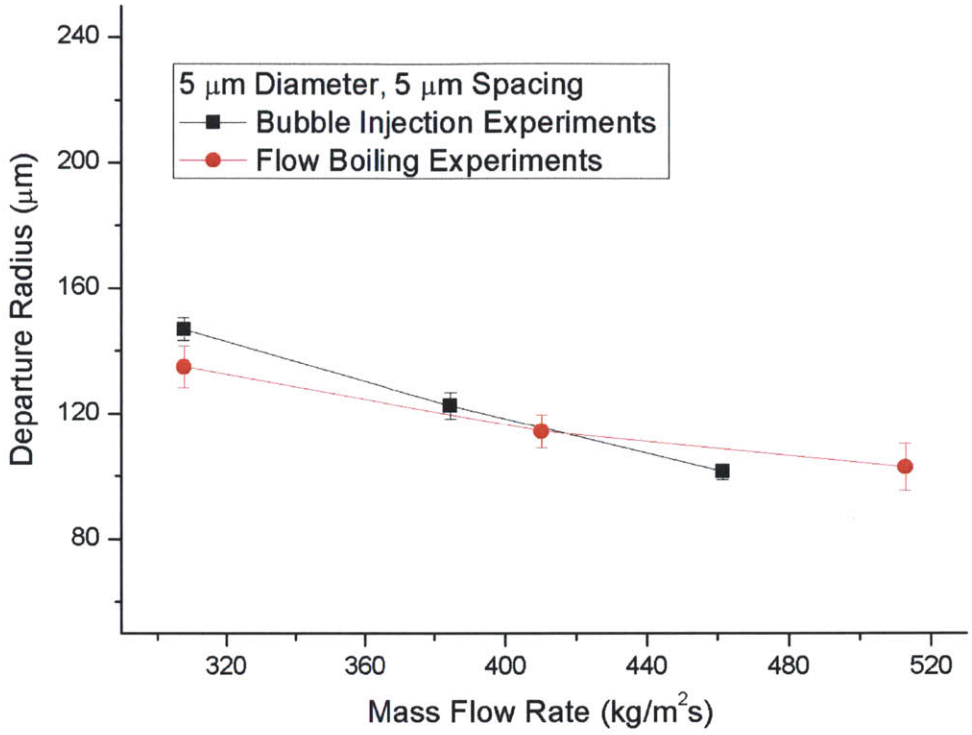

Figure 5-9 Comparison of bubble departure radius between injection experiments and flow boiling experiments.

5.5 Chapter Summary

In this chapter, an experimental setup to observe the bubble departure behaviors on a silicon micropillar array surface was presented. Bubble departure sizes on different surfaces at various flow rates were measured. It was found that a plain surface has smaller departure sizes than those of micropillar array surfaces. Comparing the departure size among the micropillar array surface, the experimental results showed that the surfaces with solid fractions greater than 0.162 had larger departure sizes than that of surfaces with solid fractions smaller than 0.162 at mass flow rates above 250 kg/m^{2}s while departure sizes of the higher solid fraction surfaces become smaller than that of lower solid fraction surfaces when flow rates decreased

below 200 kg/m^{2}s. The channel size effect on bubble departure size was studied and it was found that a smaller channel had smaller departure sizes. The comparison between bubble departure sizes obtained by air injection experiments and flow boiling experiments has also been done and the similarity of departure size obtained by both methods indicates the results of this air injection experiment could provide useful information for understanding the bubble departure behaviors on pillar array micropillar array surfaces.

Chapter 6

Conclusions and Future Work

In this thesis, a model was developed to predict the bubble morphology on micropillar array surfaces. The results showed that on high solid fraction surfaces, a bubble tends to stay on the top of pillars, keeping a liquid film underneath the bubble; on low solid fraction surface, the bubble tends to propagate within pillar structures. For the silicon pillar array surfaces, the critical solid fraction is found to be 0.162. For surfaces with higher solid fraction than this critical solid fraction, a Cassie-Wenzel mixture bubble is more likely to form. The mode in this thesis could give some suggestions on design of the structured surface, as a Cassie-Wenzel mixture bubble is more preferable for heat transfer due to the liquid thin film that forms underneath the bubble.

A flow loop with good degassing and precise fluid temperature control system was designed and built in this work. A test fixture that allows observing bubble dynamics in microchannels under flow boiling condition was demonstrated and experiments were conducted to explore the bubble dynamics on pillar array silicon surfaces. Four bubble departure modes were found during the experiments and preliminary results showed that the bubble departure behaviors vary among those modes. Three potential methods were also introduced to create single nucleation sites on pillar array surfaces for better understanding how surface structures affect bubble dynamics.

An experiment setup for observing departure behaviors of bubbles created by air injection was presented. The bubble departure radii on the pillar array surfaces and a plain surface for comparison were measured at various flow rates. The results showed that the plain surface had smaller departure sizes than other structured surfaces. The surfaces with a high solid fraction had larger bubble departure sizes in high flow rates, while they had smaller bubble departure sizes in low flow rates compared to the surfaces with a low solid fraction. The channel size's effect on bubble departure size was studied and it was found that smaller channels will have smaller departure sizes. The comparison between bubble departure sizes obtained by air injection experiments and flow boiling experiments was also done and the

similarity of departure size obtained by both methods indicated that the results of this air injection experiment could provide useful information for understanding the bubble departure behaviors on pillar array surfaces.

6.1 Recommendation for Future Work

Creating a single nucleation site on a structured surface is important for experimentally explore the bubble dynamics on structured surfaces. One potential direction for future work could focus on creating a single nucleation by chemically changing the surface property of a small area on a structured surface from hydrophilic to hydrophobic. Using the 5 μm tip covered with Epoxy to contaminate a single pillar unit and then cure the Epoxy is suggested here as it is the easiest method to do. Creating a high aspect ratio hole by FIB may also be an effective way to create a nucleate site. However, the method itself is very complicated and time consuming.

The next suggestion for future work may focus on bubble growth rate and heat transfer coefficient measurements on different pillar array surfaces. As the model predicts, a high solid fraction surface may possibly form a Cassie-Wenzel mixture bubble, which introduces a lot of liquid thin film underneath the bubble. These liquid thin films are good for heat transfer and the high solid fraction surface is expected to have a high bubble growth rate and a high heat transfer coefficient.

Bubble interactions may also be an effective way to remove the bubble from the surface. Interactions could happen between two growing bubbles and a growing bubble with a departed bubble. Interactions may be enhanced on surfaces with higher nucleation density. Future work may also focus on how surface structures affect bubble departure behavior due to the bubble interaction, which possibly could give useful information on designing the surfaces for easier bubble departure due to the bubble interaction.

7. Bibliography

[1] Kurtz, *Opportunities and Challenges for Development of a Mature Concentrating Photovoltaic Power Industry*, National Renewable Energy Laboratory, Technical Report, NREL/TP-520-43208, 2009.

[2] Peharz *et al., Investigations on the temperature dependence of CPV modules equipped with triple-junction solar cells*, Progress in Photovoltaics: Research and Applications, 2011.

[3] Kinsey *et al., Concentrator multijunction solar cell characteristics under variable intensity and temperature*, Progress in Photovoltaics: Research and Applications, 2008.

[4] Pop, *Energy Dissipation and Transport in Nanoscale Devices*, Nano Research 3, 147, 2010.

[5] Krishnan *et al, Towards a Thermal Moore's Law*. IEEE Transactions on advanced packaging, Vol. 30, No. 3, 2007.

[6] Mukherjee *et al., Smart, Low-cost, Pumpless Loop for Micro-channel Electronic Cooling Using Flat and Enhanced Surfaces*, Inter Society Conference on Thermal Phenomena, 2002.

[7] Qu *et al., Measurement and Correlation of Critical Heat Flux in Two-phase Micro-channel Heat Sinks*, International Journal of Heat and Mass Transfer 47 (2004) 2045-2059.

[8] Wojtan *et al., Investigation of saturated critical heat flux in a single, uniformly heated microchannel*, Experimental Thermal and Fluid Science, 30 (2006) 765-774.

[9] Bergles *et al., On the Nature of Critical Heat Flux in Microchannel*, Journal of Heat Transfer, 2005, Vol. 127/101.

[10] Boure *et al., Review of Two-phase Flow Instability*, Nuclear Engineering and Design, 25(1973) 165-192.

[11] Kuo *et al., Flow Boiling Instabilities in Microchannels and Means for Mitigation by Reentrant Cavities*, Journal of Heat Transfer, 2008, Vol. 130/072402-1.

[12] Kandlikar *et al., Experimental Evaluation of Pressure Drop Elements and Fabricated Nucleation Sites for Stabilizing Flow Boiling in Minichannels and Microchannels*, 3rd International Conference on Microchannels and Minichannels, 2005.

[13] Kosar *et al., Suppression of Boiling Flow Oscillations in Parallel Microchannels by Inlet Restrictors*, Journal of Heat Transfer, 2006, Vol. 128/251.

[14] Park *et al., Effect of Inlet Orifice on Saturated CHF and Flow Visualization in Multi-microchannel Heat Sinks*, 25th IEEE SEMI-THERM Symposium, 2009.

[15] Kandlikar, *Nucleation Characteristics and Stability Considerations during Flow Boiling in Microchannels*, Experimental Thermal and Fluid Science, 30 (2006) 441-447.

[16] Kuo *et al., Flow Boiling Instabilities in Microchannels and Means for Mitigation by Reentrant Cavities*. Journal of Heat Transfer, July 2008, Vol. 130.

[17] Li *et al, Enhancing Flow Boiling Heat Transfer in Microchannels for Thermal Management with Monolithically-Integrated Silicon Nanowires*, Nano Letters, 2012.

[18] Lee *et al., Bubble Dynamics in Microchannels. Part I: Single Microchannel*, International Journal of Heat and Mass Transfer, 47 (2004) 5575-5589.

[19] Li *et al., Bubble Dynamics in Microchannels. Part II: Two Parallel Microchannels*, International Journal of Heat and Mass Transfer, 47 (2004) 5591-5601.

[20] Kuo *et al.*, *Bubble Dynamics During Boiling in Enhanced Surface Microchannels*, Journal of Microelectromechanical Systems, 2006.
[21] Bico *et al.*, *Rough Wetting*, Europhysics Letters, 2001.

Appendix A

Design of the Degassing Tank (unit: inch)

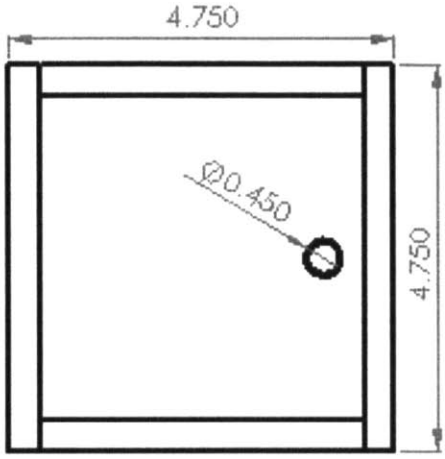

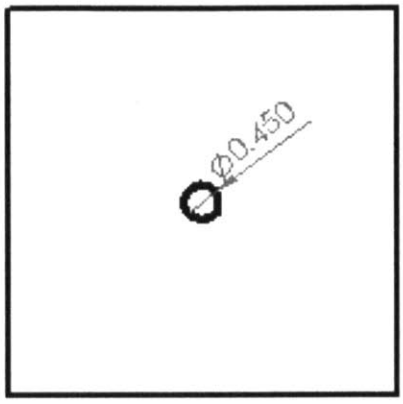

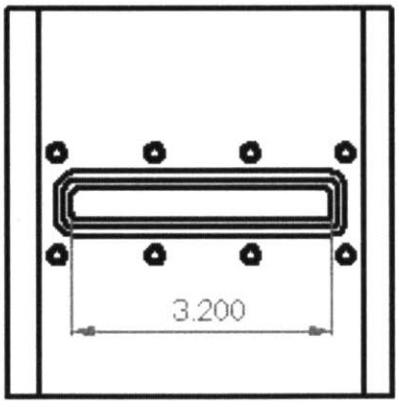

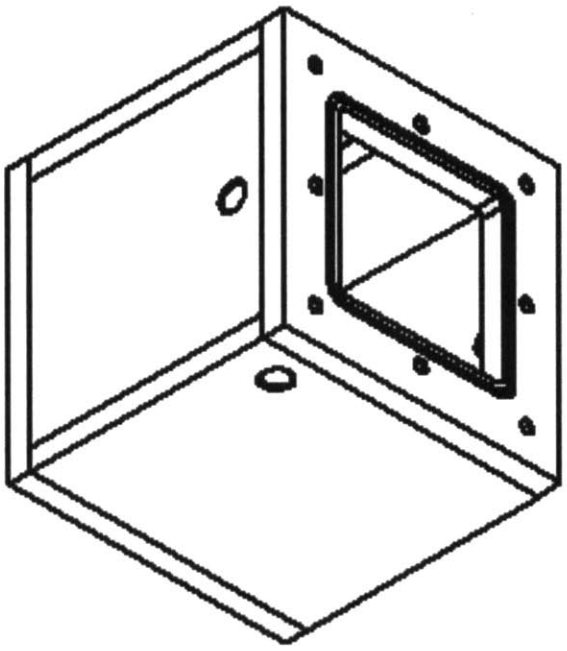

Appendix B

Design of the Test Fixture for Flow Boiling in A Microchannel (unit: inch)